Precipitation Science

Measurement, Remote Sensing, Microphysics, and Modeling




Edited by

Silas Michaelides

ELSEVIER

Precipitation Science

Measurement, Remote Sensing, Microphysics, and Modeling

Edited by

Silas Michaelides

Climate and Atmosphere Research Center (CARE-C),
The Cyprus Institute, Nicosia, Cyprus

ELSEVIER

Elsevier
Radarweg 29, PO Box 211, 1000 AE Amsterdam, Netherlands
The Boulevard, Langford Lane, Kidlington, Oxford OX5 1GB, United Kingdom
50 Hampshire Street, 5th Floor, Cambridge, MA 02139, United States

British Library Cataloguing-in-Publication Data
A catalogue record for this book is available from the British Library

Library of Congress Cataloging-in-Publication Data
A catalog record for this book is available from the Library of Congress

ISBN: 978-0-12-822973-6

For Information on all Elsevier publications
visit our website at https://www.elsevier.com/books-and-journals

Publisher: Candice Janco
Acquisitions Editor: Amy Shapiro
Editorial Project Manager: Sara Valentino
Production Project Manager: Sruthi Satheesh
Cover Designer: Mark Rogers

Typeset by MPS Limited, Chennai, India

CHAPTER

The potential of using satellite-related precipitation data sources in arid regions

7

Mona Morsy[1,2,3], Peter Dietrich[3,4], Thomas Scholten[2], Silas Michaelides[5], Erik Borg[6,7] and Youssef Sherief[8,9]

[1]*Geology Department, Faculty of Science, Suez Canal University, Ismailia, Egypt*

[2]*Department of Geosciences, Soil Science and Geomorphology, University of Tübingen, Tübingen, Germany*

[3]*Department Monitoring-und Erkundungstechnologien Helmholtz-Zentrum für Umweltforschung—UFZ, Leipzig, Germany*

[4]*Geo-und Umweltforschungs-zentrum (GUZ), Umwelt-und Ingenieurgeophysik, Tübingen, Germany*

[5]*Climate and Atmosphere Research Center (CARE-C), The Cyprus Institute, Nicosia, Cyprus*

[6]*German Aerospace Center, German Remote Sensing Data Center, National Ground Segment, Neustrelitz, Germany*

[7]*Geoinformatics and Geodesy, Neubrandenburg University of Applied Sciences, Neubrandenburg, Germany*

[8]*Geography Department, Faculty of Arts and Social Sciences, Sultan Qaboos University, Muscat, Oman*

[9]*Geography Department, Faculty of Arts, Zagazig University, Zagazig, Egypt*

Chapter Outline

Precipitation Science. DOI: https://doi.org/10.1016/B978-0-12-822973-6.00001-9

7.1 Arid regions

Arid regions are defined as areas receiving only light and irregular precipitation, with rates falling below those of evaporation. In contrast, semiarid regions are those receiving a relatively greater amount of precipitation, which can occur for several months out of the year and allow soil moisture to reach levels that can support grass and shrubland (Ezzahar et al., 2007). As described by Pilgrim et al. (1988), the degree of aridity can be determined by calculating the ratio of mean annual precipitation to mean annual evaporation. This degree helps define distinct aridity zones, such as semiarid, arid, and hyperarid. Their means can vary considerably, with semiarid zones presenting a ratio of 0.20−0.50, arid zones a ratio of 0.03−0.20, and hyperarid falling to 0.03 or below. Regions characterized as arid or semiarid display greater climate instability and variation than hyperarid zones Depending on the season, they can experience both drought and flooding, which leads to environmental disasters as well as severe water shortages that heavily stress local aquifers.

Arid and semiarid regions represent 30% of the world's terrestrial area (Dregne et al., 1991). These areas have recently experienced a rapid increase in population density, with over one billion inhabitants globally (Yin et al., 2013). This increase has led to higher land cover and usage, pressures that both local governments and international scientific communities are carefully monitoring.

7.2 Challenges of arid regions

7.2.1 Water scarcity

Increased freshwater demand has become a growing problem in arid and semiarid zones. Population growth in these areas has surpassed that of more humid regions, despite local water supply being much lower. In fact, the majority of arid and semiarid areas worldwide rely mainly on groundwater that is primarily recharged by rainfall. This recharge, however, is infrequent and unpredictable, with precipitation occurring only once or twice per year. This insufficient recharge in turn lowers the quality of available groundwater and leads to increased salinization.

7.2.2 Data scarcity

Data availability is a limiting factor when deriving scientific conclusions of studies on arid and semiarid regions, with insufficient data reducing the quality of results and leading to misguided decisions and policies. Data influencing these regions can be divided into two groups, both of which can be difficult to estimate. These consist of natural and man-made factors. Natural factors are those influencing the water cycle and directly include precipitation rate, evapotranspiration, runoff, and infiltration. Indirect factors include temperature, relative humidity, and wind speed (Sherief, 2008). In contrast, man-made factors can describe, for example, water consumption rate, population expansion, land cover increase, and intensification of land use.

Collecting sufficient usable data on the abovementioned factors is critical for sustainable groundwater management in arid and semiarid zones. However, rain gauges in most mountainous arid regions are few and sparse, if present at all (Poméon et al., 2018). Additionally, these existing gauges have a limited capability for capturing continuous records (e.g., hourly changes might not be recorded). Furthermore, the gauges are largely isolated and represent areas of low population density (Pilgrim et al., 1988), which results in a low frequency of maintenance and rapid deterioration. Taken together, these factors significantly reduce the efficacy of water management strategies in arid areas, affecting the water table and general development in the region.

7.3 The water cycle in arid regions

Adequate management of water resources has recently become an issue of intense focus on arid and semiarid regions. The local freshwater supply in these climate zones is generally highly limited and is mainly derived from groundwater, which is susceptible to depletion (Sheffield et al., 2018). Consequently, the initial step toward sustainable groundwater control is an assessment of local water cycle equilibrium, in combination with identification of groundwater consumption rates. The results of such studies can be used to inspire rules and regulations for the maintenance and preservation of groundwater sources in semiarid areas. Potential regulations could, for example, mandate that withdrawal from aquifers do not exceed natural recharge rates, which would in turn reduce land use and limit population growth. The current chapter approaches this issue through a discussion of the water cycle, water storage, and water consumption patterns in arid and semiarid regions.

In general, the hydrological cycle describes the movement of water between the biosphere, atmosphere, lithosphere, and hydrosphere (Kuchment, 2004; Pagano & Sorooshian, 2002). Fresh water can accumulate and be stored in various natural reservoirs, such as oceans, lakes, rivers, soil, glaciers, groundwater, and the atmosphere. Water is also able to transfer between reservoirs by precipitation, evaporation, condensation, deposition, runoff, and infiltration (Kuchment, 2004). The reservoirs contributing most to evaporation are the oceans, where water vapor transfers to the atmosphere in the form of clouds that are then propelled great distances by wind, before finally condensing and precipitating, furthering the cycle (Pagano & Sorooshian, 2002). Although wind can promote the transportation of cloud water, the vast majority (91%) of precipitation occurs over the oceans themselves. The other 9% of precipitation falls over land masses, where it then either infiltrates the ground or becomes surface runoff (Kuchment, 2004; Pagano & Sorooshian, 2002). This precipitation can result in three general outcomes: replenishment of atmospheric water reservoirs via evaporation, recharging of groundwater, or returning to the ocean (Kuchment, 2004; Pagano & Sorooshian, 2002). The balance of water entering and exiting a particular environment can be described as its water cycle equilibrium. Taking into account multiple factors affecting water availability, this can be quantified by the following formula (Han et al., 2010; Niu et al., 2007; Pitman, 2003):

$$P = E + R + \Delta S \tag{7.1}$$

where P represents the rate of precipitation, E is the rate of evapotranspiration, R is the amount of runoff, and ΔS is the change in storage capacity of soil moisture. In recent decades, exploitation of groundwater has intensified as a result of climate change and global warming. This has led to alterations in local hydrological cycles that are increasingly destabilizing regional water balances (Shen & Chen, 2010).

7.3.1 Precipitation

Precipitation functions as the primary factor maintaining water cycle equilibrium [Eq. (2.1)]. Accordingly, it has served as a dominant subject in the majority of hydrological studies on flash flood risk assessment, groundwater localization, climate change, and forecasting (Tapiador et al., 2012).

7.3.2 Infiltration

Infiltration describes the first hydrological consequence of precipitation, occurring when rainfall hits the ground and percolates the soil surface (Beven, 2004; Thornes, 2009). Several factors controlling rainfall percolation rate and its spatial variability include soil type, texture, moisture, and hydraulic properties; vegetation; animal activities; and climate (Beven, 2004; Khan et al., 2014). Infiltration and runoff in arid and semiarid regions display more complex characteristics when compared with less dry climates, as several additional factors exist that influence the two. For example, they can be affected by the relationship between bedrock slope, curvature, porosity, permeability, and extent versus the degree of soil cover (Beven, 2004; Khan et al., 2014). To semiquantify infiltration, internationally documented models incorporate several of these aforementioned factors (e.g., bedrock qualities and soil cover) as input parameters (Khan et al., 2014).

7.3.3 Runoff

Runoff is defined as the outflow of precipitated water from landmasses to the open ocean. As described by Dyck et al. (1980), runoff occurs when the precipitation of a rainfall event is greater than the infiltration capacity of the affected soil. This can be due to several reasons, such as soil saturation, or the closing off of openings in the soil. As a hydrological phenomenon, it produces both constructive and destructive consequences. Its presence can negatively affect settlements, vegetation cover, road infrastructure, and, in some cases, lead to soil erosion and devastating landslides. Alternatively, it can also be exploited as a source of fresh water in arid regions. In fact, it is a recent target of interest for addressing the increasing demand for potable water and electricity in these areas (Massoud et al., 2010). To quantify the relationship between rainfall and runoff, researchers utilize several techniques, among them: simple correlation, area-based methods, regional regression methods, and Geographic Information System (GIS)-based models (Abuzied et al., 2016; Bo et al., 2011; Massoud et al., 2010). These models are based on water cycle equilibrium and incorporate land use, soil type, terrain slope, soil moisture, and antecedent moisture as primary input parameters (Horton, 1941).

7.3.4 Evapotranspiration

Evapotranspiration concerns the movement of water and energy from the lithosphere and hydrosphere to the atmosphere (Li et al., 2014). Evapotranspiration consists of two processes: the evaporation of liquid water from landmasses and large water bodies and the transpiration of water from plant leaves (Vinukollu et al., 2011). Evapotranspiration strongly influences water cycle equilibrium, especially in arid and semiarid regions, where the evaporation rate can regularly exceed the precipitation rate. Consequently, estimation and semiquantification of evapotranspiration is another target of focus when determining strategies for efficient water resource management in arid areas (Shen & Chen, 2010). Unfortunately, data on evapotranspiration cannot be retrieved directly by remote sensing products (Kalma et al., 2008). It can, however, be estimated by its dependence on various factors, namely local temperature, relative humidity, wind speed, vegetation characteristics, and plant phenology (Kalma et al., 2008). As a result, the estimation of evapotranspiration requires input from a variety of sensors, ground observations, and models (Kalma et al., 2008; Kustas & Norman, 1996).

7.4 Storage

The global availability of stored water can be separated into distinct reservoirs, including both on- and in-land freshwater resources. Among the on-land sources are glaciers, snow, lakes, marshes, and rivers. In-land freshwater resources, on the other hand, exist as soil moisture and groundwater (Hartmann et al., 2002). The amount of global water supply that is stored on- and in-land is relatively small, though the water flux through these systems is relatively great (Hartmann et al., 2002; Pagano & Sorooshian, 2002). In the majority of arid regions, aquifers represent the predominant source of stored fresh water, and storage rate depends mainly on aquifer type, water table level, and degree of water flux (Hartmann et al., 2002; Pagano & Sorooshian, 2002).

7.4.1 Aquifers

Aquifers serve as the primary in-land reservoirs of stored fresh water in arid and semiarid regions. They can be categorized into three distinct types: confined, unconfined, and leaky aquifers (with the type depending mainly on the local lithology). Confined aquifers are both over- and underlaid by a confining bed and yield usable quantities of fresh water to wells or springs (Heath, 1983). Unconfined aquifers, in contrast, are overlaid by permeable beds and underlaid by confining beds with very low hydraulic conductivity (Heath, 1983; Prasad, 2002). Leaky aquifers are overlaid or underlaid by a semipermeable layer through which vertical leakage can take place (Prasad, 2002).

Water stored by aquifers in arid areas can originate as either “modern” or “fossil” groundwater (Sultan et al., 2011), two types distinguishable by distinct isotopic signatures. Modern water describes water that recharges aquifers during current and ongoing precipitation events. Fossil groundwater, however, is that which formerly recharged the aquifer during previous decades under different climatic conditions (Sultan et al., 2011). Naturally, the majority of recent precipitation in currently arid regions tends to limited and low in intensity. It insufficiently recharges local aquifers and cannot provide for the increasing water demands of growing populations, shifting reliance toward fossil groundwater.

7.4.2 Soil moisture

The secondary reservoir for in-land water storage derives from soil moisture, which is responsible for the interaction between the lithosphere and atmosphere. It is considered to be one of the most critical variables for determining climate (Parinussa et al., 2017). This variable is often used to highlight the differences between drought and flood seasons (Cao et al., 2019) and is required for the modeling of important hydrological factors, such as infiltration and runoff (Parinussa et al., 2017). Soil moisture displays high temporal variation, as well variation between topographies, soil properties, vegetation, and climate (Crow et al., 2012). To obtain continuous data on soil moisture, scientists use in situ measurements along with microwave sensors to produce datasets with considerable accuracy and spatial resolution, as well as a high capture frequency (Liu et al., 2012).

7.4.3 Rivers and lakes

On-land reservoirs of stored water consist of rivers and lakes. Furthermore, there exists a hydraulic interaction between surface and groundwater in many watersheds, with streams, rivers, and lakes both feeding and withdrawing from the local groundwater aquifer (Kuchment, 2004; Pagano & Sorooshian, 2002). The entire process depends on the aquifer groundwater level that itself is reliant on both precipitation and irrigation rate (Massoud et al., 2010). However, if water inflow and outflow are under equilibrium, the absolute change in water storage will be zero. While rivers and lakes are uncommon in arid regions, aquifers can occasionally lie adjacent to seaside coastlines. Hydraulic connection between the two can lead to issues with water contamination and saltwater intrusion, especially when groundwater levels drop below those of the sea surface (Eissa et al., 2016). In such situations, limits on water withdrawal should be implemented to avoid these consequences, taking precipitation and water recharge rates into consideration.

7.5 Water consumption

Water consumption is the driving force unbalancing the water budget in arid regions. Consumption rates gradually but directly increase with population mass and subsequent land cover and land development (Scanlon et al., 2006). As a result, it is critical for the continuity of arid communities that population (and consequently water withdrawal) are limited.

Precisely 6% of the world's forests are located in arid zones (Malagnoux, 2007) and, despite natural climate constraints, are increasingly being used for agriculture. In fact, 85% of available water in these regions is diverted for crop irrigation (Ezzahar et al., 2007). To combat this, several projects have been established for the promotion of sustainable management of irrigation water in arid climates (Malagnoux, 2007).

One billion people reside in arid regions worldwide and as a group represent the world's poorest (Malagnoux, 2007). As this population grows and water needs increase, the overexploitation of trees and forests required to sustain the population will lead to further desertification. Additionally, reduced rainfall due to climate change and global warming will fail to adequately recharge aquifers, also leading to the insufficient natural irrigation of the abovementioned forests (Malagnoux, 2007).

Precipitation serves as the key parameter of water cycle equilibrium in arid regions, primarily due to its role in recharging ground aquifers and compensating for human consumption. Rain gauges are the most accurate tools for measuring both precipitation rate at a physical point scale and rainfall depth as it accumulates overtime (Sun et al., 2018; Tapiador et al., 2012). Several types of rain gauges exist, including accumulation gauges, tipping bucket gauges, weighing gauges, and optical gauges, each with their own strengths and weaknesses (Sun et al., 2018; Tapiador et al., 2012). The most commonly used type is the tipping bucket gauge that is used to estimate rainfall rate and volume. It has the capability to measure trace amounts of rain, as little as 0.2, 0.5, or 1 mm (Das & Prakash, 2011). The instrument consists of a funnel that receives the rain and sections it into smaller containers. These containers then dump the rainwater collecting a certain quantity. The dumping procedure is accompanied by an electrical signal that is recorded. In older versions, this signal would be recorded by a pen mounted on an arm attached to a geared wheel (Das & Prakash, 2011). However, tipping bucket gauges do contribute a source of error when measuring heavy rainfall, as the water can accumulate in the containers faster than the dumping process can take place, leading to an underestimation of the heavy rainfall rate. This can occur when the precipitation rate is higher than 300 mm h^{-1}. This type of gauge can also underestimate a light rainfall rate when water evaporates out of the containers prior to the dumping step (Das & Prakash, 2011). A less commonly used type of rain gauge depends on the weighing of the rainfall accumulated at different sampling rates. The saturation effect is therefore not relevant (Tapiador et al., 2012). One of the challenges faced when attempting the accurate estimation of rainfall rate by rain gauges in arid regions is the wind effect, especially during light rainfall. Wind can transfer these sparse raindrops between locations, disturbing the point scale measuring function of the rain gauges. This can lead to two gauges in close proximity recording different quantities of rainfall (Tapiador et al., 2012).

7.6 Satellite-based precipitation data sources

Ground-based rain gauges are traditionally used to measure precipitation by measuring an incremental mass of accumulated rainfall as a function of time. However, the existing network of rain gauges is far from satisfactory in resolving the spatiotemporal characteristics of precipitation. Although this knowledge gap is partly bridged via the use of other ground-based instruments (e.g., disdrometers, ground-based radars), sensors onboard satellites are currently the only instruments that can provide global and homogeneous precipitation measurements. Michaelides et al. (2009) provide a comprehensive discussion of ground- and space-based precipitation measurement instruments.

The precipitation sensors onboard of Earth-orbiting satellites are broadly classified into three categories: (1) visible and infrared (IR) sensors on geostationary orbit (GEO) and low Earth orbit (LEO) satellites, (2) passive microwave (PMW) sensors on LEO satellites, and (3) active microwave (AMW) sensors on LEO satellites (see Prigent, 2010). Retrieval methods used to quantitatively estimate precipitation from satellite-based sources have been developed. Kidd and Levizzani (2011) provide a review of quantitative precipitation estimation, covering the basics of the satellite systems used in the observation of precipitation, the dissemination and processing of this data, and the generation, availability, and validation of the precipitation estimates.

Different sources of satellite-related precipitation data with varying spatial resolution and capturing frequency have been used to determine the spatiotemporal characteristics of precipitation in numerous applications. Sun et al. (2018) present a comprehensive review of data sources and estimation methods of several currently available global precipitation datasets, including gauge-based, satellite-related, and reanalysis datasets; Table 7.1, which is based on their work, summarizes the major satellite-related precipitation data sources (Adler et al., 2003, 2018; Ashouri et al., 2015; Beck et al., 2017; Hou et al., 2008, 2014; Huffman et al., 2007, 2020; Joyce et al., 2004, 2010; Maidment et al., 2014, 2017; Sorooshian et al., 2000; Ushio et al., 2009; Xie et al., 2003, 2010).

In this section the two satellite-related data sources that are used in the following statistical analysis of their potential application over an arid region are outlined. The first of these two datasets is the TMPA [Tropical Rainfall Measuring Mission (TRMM) Multisatellite Precipitation Analysis] and the second is the IMERG (Integrated Multi-Satellite Retrievals for Global Precipitation Measurement, GPM).

Huffman et al. (2007, 2010) describe the two major sources of data input to TMPA. The first source of input data for the TMPA consists of precipitation-related PMW data that are collected by a variety of LEO satellites. The TRMM provided data for the estimation of rainfall in tropical and subtropical areas (Chen et al., 2018; Kim et al., 2017). It was a joint space mission between the US National Aeronautics and Space Administration (NASA) and the Japan Aerospace Exploration Agency (JAXA) (Fensterseifer et al., 2016; Kummerow et al., 1998). The TRMM carried onboard five instruments: a Precipitation Radar (PR, operating at 13.8 GHz), a TRMM Microwave Imager (TMI, a nine-channel PMW radiometer), a visible IR scanner (VIRS, a five-channel visible/IR radiometer), a Clouds and Earth's Radiant Energy System (CERES), and a lightning imaging sensor. PR operated as one transmitting/receiving frequency and one polarization, providing information about rain type, strength, and distribution (Kummerow et al., 1998). The TMI provided quantitative information about rainfall, water vapor, cloud water content, and sea surface temperature (Immerzeel et al., 2009; Kummerow et al., 1998). The PR complemented the results of the TMI and PMW sensors to provide measurements of radiance through precipitating clouds along the sensor view path. Radiance frequency reflects the properties of clouds and precipitation particles (Guo et al., 2017). The AMW sensors provided information about cloud height by measuring the backscatter delay (Guo et al., 2017). The VIRS provided indirect measurements of rainfall intensity, distribution, and type

Table 7.1 Major satellite-related precipitation data sources (based on Sun et al., 2017).

Satellite-based source	Resolution	Frequency	Coverage	Period	References
GPCP	2.5°	Monthly	Global	1979–present	Adler et al. (2003)
GPCP1dd	1.5°	Daily	Global	1979–present	Adler et al. (2018)
GPCP_PEN_v2.2	2.5°	5-daily	Global	1979–2014	Xie et al. (2003)
CMAP	2.5°	Monthly	Global	1979–present	Xie et al. (2003)
CPC-Global	0.5°	Daily	Global land	2006–present	Xie et al. (2010)
TRMM3B43	0.25°	Monthly	50°S–50°N	1998–present	Huffman et al. (2007)
TRMM3B42	0.25°	3 h/daily	50°S–50°N	1998–present	Huffman et al. (2007)
GSMaP	0.1°	1 h/daily	60°S–60°N	2002–12	Ushio et al. (2009)
PERSIANN-CCS	0.04°	30 min/3, 6 h	60°S–60°N	2003–present	Sorooshian et al. (2000)
PERSIANN-CDR	0.25°	3, 6 h/daily	60°S–60°N	1983–present	Ashouri et al. (2015)
CMORPH	0.25°/8 km	30 min/3 h/Daily	60°S–60°N	2002–present	Joyce et al. (2004, 2010)
GPM	0.1°	30 min/3 h/daily	60°S–60°N	2015–present	Hou et al. (2008, 2014), Huffman et al. (2020)
MSWEP & CHIRPS	0.1°/0.5°	3 h/daily	Global	1979–present	Beck et al. (2017)
TAMSAT	0.04°	Daily	Africa	1983–present	Maidment et al. (2014, 2017)

Source: *From Sun, Q., Miao, C., Duan, Q., Ashouri, H., Sorooshian, S., & Hsu, K. L. (2018). A review of global precipitation data sets: Data sources, estimation, and intercomparisons.* Reviews of Geophysics, 56*(1), 79–107. https://doi.org/10.1002/2017RG000574.*

(Fensterseifer et al., 2016; Kummerow et al., 1998). The VIRS provided less reliable data on its own (Guo et al., 2017); however, it provided more frequent data when compared to the infrequent data captured by the TMI and PR. The lightning sensor played an important role in connecting lightning occurrence to precipitation events, while CERES allowed for the determination of the total radiant energy balance. Analyzed together with the latent heating derived from precipitation, it was then possible to construct a significantly improved picture of our atmospheric energy system (Kummerow et al., 1998). A special sensor microwave/imager (SSM/I) onboard the Defense Meteorological Satellite Program collects data regarding the Earth's atmosphere through its microwave instrument (Alemohammad et al., 2014). The microwave radiometer is passive and has the capability of measuring radiation emitted at four frequencies, in both ascending and descending overpasses. SSM/I provides valuable information on precipitation rate, water vapor, cloud liquid water, wind speed, and soil moisture (Berg et al., 2012). Additional sources of microwave data are the Advanced Microwave Scanning Radiometer-Earth Observing System onboard Aqua, and the Advanced Microwave Sounding Unit-B onboard the National Oceanic and Atmospheric Administration satellite series. The second major source for the TMPA consists of data from the international constellation of GEO satellites and, in particular, in the IR channel ($\sim$10.7 μm).

TMPA provided some of the most recommended and used satellite-related data sources (Abera et al., 2016; Retalis et al., 2018). It allowed for high spatiotemporal coverage, despite some uncertainties due to cloud effects as well as limitations in remote sensor performance and retrieval algorithms (Long et al., 2016). The data are available from 50°S to 50°N with a relative bias of 2.37% (Fensterseifer et al., 2016).

The GPM mission is an international network of satellites that provide the next-generation global observations of rain and snow. The foundation of the GPM mission is the Core Observatory (CO). Data collected from the CO satellite serve as a reference standard, unifying precipitation measurement from research and operational satellites launched by a consortium of GPM partners in the United States, Japan, France, India, and Europe. The CO satellite is the outcome of the recent precipitation-related collaboration between NASA and JAXA and is focused on the observation of global precipitation. The CO satellite is equipped with two sensors: the GPM Microwave Imager (GMI), which measures the intensity, type, and size of the precipitation, and the Dual-frequency Precipitation Radar (DPR), which observes the structure of storms within and under clouds (Kim et al., 2017; Libertino et al., 2016). GMI uses 13 different microwave channels ranging in frequency from 10 to 183 GHz and with resolutions ranging from 11.2 × 18.3 km to 4.4 × 7.3 km observes energy from the different types of precipitation through clouds for estimating everything from heavy to light rain and for detecting falling snow. In addition, the GMI carries four high-frequency, millimeter-wave, channels near 166 and 183 GHz. The DPR consists of a Ku-band precipitation radar and a Ka-band precipitation radar, measuring in frequencies of 13.6 and 35.55 GHz, respectively, and with a spatial resolution equal to 5×5 km, and with swath area ranging from 245 to 120 km. The IMERG algorithm (see Huffman et al. (2020)) is the Level 3 multisatellite precipitation algorithm of the GPM, which combines intermittent precipitation estimates from all constellation microwave sensors, IR-based observations from GEO satellites, and monthly rain-gauge precipitation data (Ghodeif & Gorski, 2001). Three different daily IMERG products are offered: IMERG Day 1 Early Run (near real time, with a latency of 6 h), IMERG Day 1 Late Run (reprocessed near real time with a latency of 18 h), and IMERG Day 1 Final Run (gauged-adjusted with a latency of 4 months) (Guo et al., 2016). The IMERG Final Run product provides more accurate precipitation information than the near-real-time products across GPCC-gauged regions (Ghodeif & Gorski, 2001).

The IMERG dataset now includes TRMM-era data, extending back to June 2000, rendering this dataset a valuable tool in many hydrological applications. Research in the application of the IMERG database in several sectors that require rainfall records will certainly continue in the years to come and this study is a contribution toward better assessing this valuable data source.

7.7 Performance of satellite-related precipitation estimations in an arid region

The El-Qaa Plain in the Sinai Peninsula was selected as a test site. This region was chosen for its standing as one of the most promising areas in the Sinai Peninsula for further development and in particular tourism. These prospects have already led to a gradual increase in the number of inhabitants and expansion of land exploitation. As a result, local water consumption is gradually increasing in an area where the main source of groundwater is the regional quaternary aquifer (El-Fakharany, 2016; El-Refai, 1992). This aquifer extends from Wadi Feiran to the head of Ras-Mohamed and is mainly recharged by rainfall (Wahid et al., 2016). The rainfall events in this area were previously classified by Sherief (2008) on the basis of the intensity of rainfall. In this respect, three classes of rainfall events were recognized: light, moderate, and heavy events, with intensities ranging from 0.1 to 1 mm, from 1 to 10 mm, and >10 mm, respectively. The annual frequency of each event class was 61% for light events, 34% for moderate events, and 5% for heavy events. Overall, the area receives nearly 77 mm of the annual precipitation through light rain events, 43 mm through moderate ones, and 6 mm from heavy events.

The groundwater localization in the area under study has been investigated by several authors (Ahmed et al., 2014; El-Fakharany, 2016; Rashed et al., 2007; Sauck et al., 2005; Sayed et al., 2004). Nevertheless, the local precipitation rate and spatiotemporal distribution of rainfall have been insufficiently investigated due to the limited number of rain gauges in the region.

As explained next, the existing coarse rain-gauge network over this area is not sufficient to shed light on the spatiotemporal distribution of precipitation. The case study presented here attempts to fill the knowledge gap through the exploitation of rainfall estimates from satellite missions that are capable of providing data on spatiotemporal distributions of rainfall. To demonstrate that satellite-derived data can meet this need, two sets of satellite-related rainfall data are tested and compared. The first dataset refers to the most commonly used dataset related to the TRMM; this dataset is the Multi-satellite Precipitation Analysis, Version 7 (3B42V7), hereafter denoted as TMPA (Huffman et al., 2007, 2010; Lonfat, 2004; Marchok et al., 2007; Tuleya et al., 2007); the second dataset refers to the more recent satellite rainfall measuring effort, the Global Precipitation Mission [GPM (Hou et al., 2014)], namely, the Integrated Multi-satellitE Retrievals for GPM, hereafter denoted as IMERG (Huffman et al., 2020).

The comparative performance of the TMPA and IMERG products has been investigated in different parts of the world (Chen et al., 2018; Fang et al., 2019; Wang et al., 2019; Wu et al., 2019). It should be noted that the availability of the GPM-related dataset started after the launch and operational functioning of the CO in 2015; therefore studies that make use of IMERG products have only been published recently. Manz et al. (2017) compared IMERG and TMPA in the tropical Andes, whereas Tan and Duan (2017) assessed their performance over Singapore. Xu et al. (2017) compared the two datasets against rain-gauge records in the Tibetan Plateau. Another study by Zhang et al. (2018) was carried out over the same area. A similar study was carried out by Anjum et al. (2018) over the mountainous region in Pakistan. In their study, Tan and Santo (2018) used the two datasets over Malaysia. The performance of the satellite-related analyses was also tested over the mountainous region of Northwest China (Anjum et al., 2019). Palomino-Ángel et al. (2019) compared reference and satellite-related mean daily precipitations over Northwestern South America. Zhang et al. (2019) assessed the two datasets over a humid basin in China. More recently, Retalis et al. (2020) tested the two datasets against a dense network of rain gauges over the island of Cyprus. From the previous outline of the existing literature of comparative assessments of TMPA and IMERG, it can be seen that investigators have been focusing mainly on areas where rainfall is not scarce and with a sufficient network for ground measurements in place.

It is challenging to investigate the performance of satellite-related precipitation datasets in an arid environment with the employment of a rather inadequate rain-gauge network where rainfall estimations are highly desirable. Bearing the above in mind, the case study presented in the following constitutes an example of an application of how space-based estimations of precipitation can be assessed in an arid environment. The abovementioned two satellite-related precipitation fields (namely, TMPA and IMERG) are statistically compared against ground measurements of precipitation over an arid area covered with a coarse rain-gauge network. In this respect the potential of using satellite-related precipitation data is discussed, in an effort to investigate whether these sources of precipitation data can improve the insufficient spatiotemporal precipitation distributions based on ground-based data in arid regions. To this end the study focuses on the Sinai Peninsula of Egypt (see Morsy et al., 2021).

7.7.1 The study site

The Sinai Peninsula is considered one of the most unique regions in Egypt and is known as a prime sightseeing destination, partly due to its location between the Mediterranean and Red Seas. It also contains vast natural wealth in the form of gemstones, gold, coal, and other resources. Like the majority of Egypt, it is classified as arid and semiarid and relies on groundwater as its source of fresh water. The eastern side of the Gulf of Suez is one of the most promising locations for future urban expansion and might in the future be able to house a considerable portion of the growing population, in addition to tourist accommodation. In fact, it currently is already demonstrating a gradual increase in the number of residences, along with the associated land exploitation. In terms of land geology, this eastern region features variable geological settings, with lithological units even appearing in fascinating outcrops. Moreover, aspect, slope, and elevation vary greatly, which in turn directly affect precipitation rates, evaporation, infiltration, and runoff. Additionally, the entire area of study relies primarily on a single aquifer. The eastern side of the Gulf of Suez is nearly 350-km long and 80-km wide (McClay et al., 1998). Regional formations complete the stratigraphy from Precambrian to Quaternary periods (McClay et al., 1998). It is located between latitudes 29°54′N and 27°42′N and longitudes 32°42′ and 34°06′E. In terms of urban areas the region is populated by Sharm El-Sheikh at its southern vertex, Ras Sudr and Abu Rudeis in the north, and the cities of El-Tor and Saint Catherine in the center. Middle and southern vertex of this region comprises the El-Qaa Plain, located between latitudes 28°30′ and 28°40′N and longitudes 33°17′ and 33°37′E (Sayed et al., 2004). The overall area of the El-Qaa Plain is roughly estimated to be 6070 km^2, with a maximum length of 150 km, and a maximum width of 20 km in the north (Ghodeif & Gorski, 2001). It is also the narrowest in the south (Azab & El-Khadragy, 2013). According to Sayed et al. (2004), the eastern portion of the El-Qaa Plain includes a Precambrian mountain region with varying elevations from 300 to 2624 m (Fig. 7.1). This region contains various types of igneous rocks, such as diorite, granite, metagabbro, and volcanic varieties (Han et al., 2010; Sherief, 2008). Its dominantly sedimentary sector can be found in Gabal Qabaliat in the northwestern sector, where elevation reaches approximately 250 m and where the terrain moderately slopes toward the El-Qaa Plain. It is also this northwestern site that separates the Gulf of Suez from the El-Qaa Plain. Local sedimentary outcrops include limestone, sandstone, siltstone, gypsum, and anhydrite formations. The central Plain is composed mainly of Quaternary deposits that are generally not perfectly flat and are often dissected by various wadies, alluvial fans, and terraces (Said, 1960). A study by Sherief (2008)

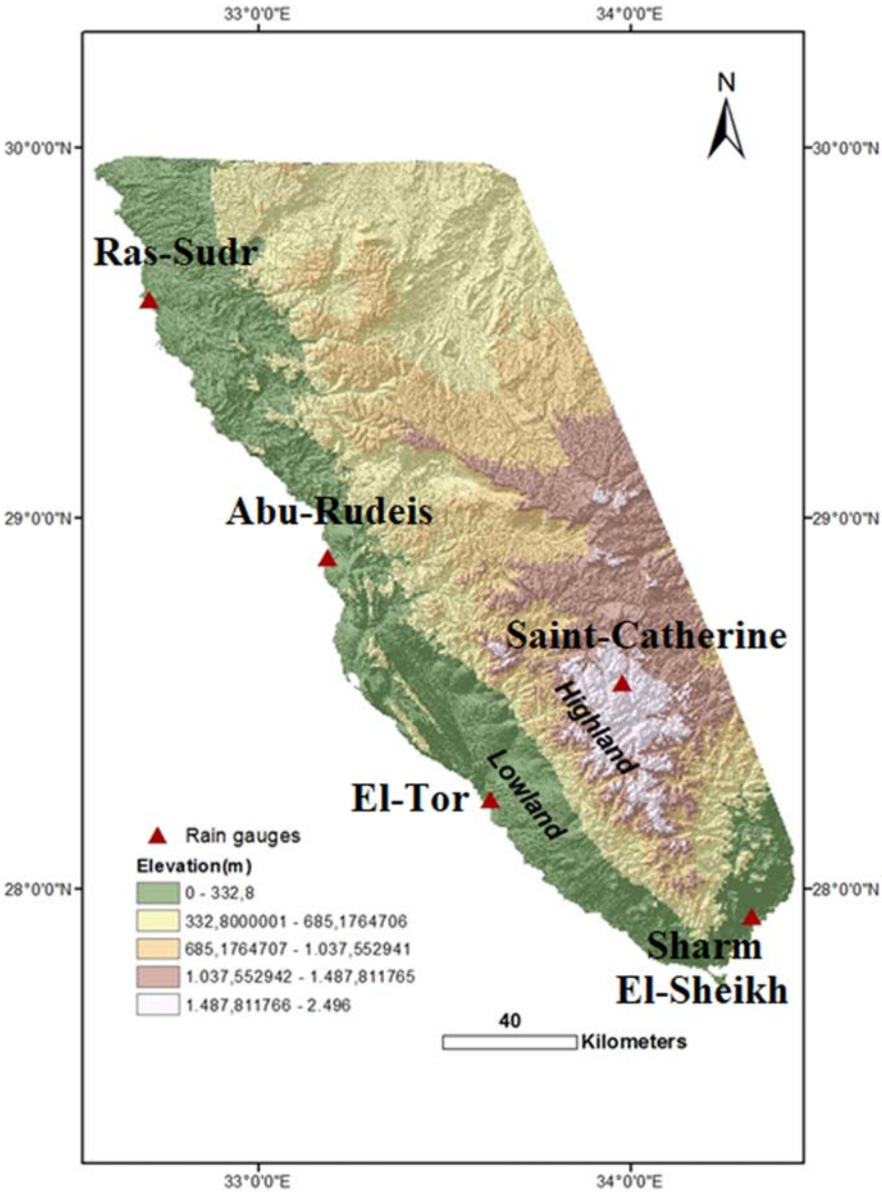

FIGURE 7.1

El-Qaa Plain is contained within the black outline with its five ground-based stations identified.

divides the area between types of deposits, whether alluvial or Wadi derived (McClay et al., 1998).

7.7.2 Rain-gauge network and in situ measurements

The study area is separated into two subareas, which are determined on their elevation: (1) the *Lowland* subarea, ranging in elevation from 0 to 300 m, includes the Ras Sudr (29.59°N, 32.71°E, 12 m) and Abu Rudeis (28.89°N, 33.18°E, 13 m) stations in the northern part of the area, the El-Tor (28.24°N,33.62°E, 13 m) station in the middle and the Sharm El-Sheikh (27.93°N, 34.32°E, 38 m) station in the South; (2) the *Highland* subarea, ranging in elevation from 300 to 2000 m, is represented by the Saint Catherine (28.55°N, 33.98°E, 1562 m) station in the middle of the area. Generally, *Highland* receives more rainfall than *Lowland*. The accumulated monthly rain-gauge measurements in the period 2015−18 are given in Fig. 7.2 for each station separately.

The Egyptian Meteorological Authority provided the in situ rain-gauge data. This data revealed the rainiest days and the number of rainy days per month for the period of 2014−18, along with the duration (in days) of each rain event. This information was then used to evaluate the performance of the data derived from the remote sensors. The most significant dates datawise were the March 9, 2014; October 25, 2015; October 27, 2016; April 12, 2017; and June 28, 2018. Data from these dates were those used to complete the statistical metrics presented next. Although the distribution and number of current rain gauges are insufficient for constructing an adequate understanding of the spatiotemporal distribution of

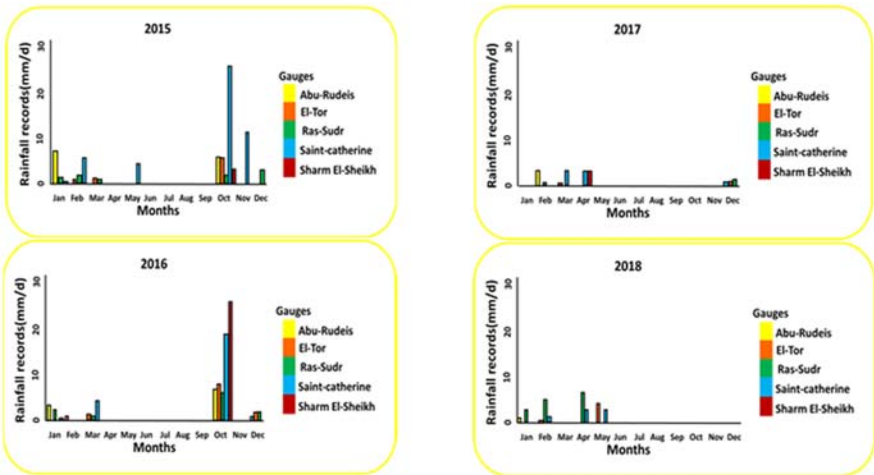

FIGURE 7.2

Monthly rain gauge records at each rain gauge station for the period of 2015−18.

rainfall at the study site, they were used in the present study as a benchmark, to gain a general idea about the accuracy of the satellite-related data, as discussed next. This was done using coherent statistical tests, to determine whether the satellite-related data tied to the test site could be used without further validation.

The first precipitation event on March 9, 2014 is ranked as a heavy intensity event, as three rain gauges recorded more than 10 mm day^{-1}, and two of them recorded 1–10 mm day^{-1}. The second event (October 25, 2015) ranked as a moderate intensity event, as three rain gauges recorded 1–10 mm day^{-1}, one rain gauge recorded $>$10 mm day^{-1}, and one gauge recorded 0.1–1 mm day^{-1}. The third event (October 27, 2016) ranked as a heavy to moderate intensity event, as two rain gauges recorded $>$10 mm day^{-1}, while three gauges recorded 1–10 mm day^{-1}. The fourth and fifth events (April 12, 2017 and June 28, 2018) ranked as light-intensity events, as the majority of gauges recorded 0.1–1 mm day^{-1}.

7.7.3 TMPA and IMERG precipitation data

For each event, eight scenes from the TRMM (TMPA) Rainfall Estimate L3 of 3-h temporal resolution and 0.25-degree spatial resolution version 7 (TRMM_3B42 7, hereafter called simply TMPA) were used in the present analysis, downloaded from the official NASA website (mirador.gsfc.nasa.gov). A GIS software was used to process the data. This was achieved in four steps complementing the first stage of the statistical metrics. The data were opened as a raster layer and clipped to match the study site. The data's pixel size was resampled to match the IMERG data. The value of each pixel was extracted and recorded in a spreadsheet, with values corresponding: the starting point of an event (0 h), 3 h later (3 h), 6 h later (6 h), 9 h later (9 h), 12 h later (12 h), and 1 day later (24 h). Subsequently, the data were divided into those corresponding to the *Lowland* and *Highland* groups, on the basis of the elevation of the area represented by the pixel. The values of the pixels whose locations coincided with those of the rain gauges were entered into a spreadsheet on a daily basis, at both the 0.25- and 0.1-degree resolutions.

A total of 50 daily scenes of GPM IMERG Final Precipitation L3 with half-hour temporal resolution and 0.1-degree spatial resolution version 06 (GPM_3IMERGHH 06, hereafter simply called IMERG) data were downloaded to encompass the previous rainy events from 2015 to 2018. This did not include data from 2014, as the GPM mission had yet to officially start. Therefore the 2014 event was excluded from the relevant statistical metrics. The official NASA website (mirador.gsfc.nasa.gov) was also used to download the scenes. The data were opened and clipped using the GIS software. The value of each pixel from the 0-, 3-, 6-, 9-, 12-, and 24-h scenes was calculated and stored in a spreadsheet. Next, the values of pixels whose locations coincided with those of the rain gauges were collected in a separate spreadsheet for further statistical treatment.

Precipitation maps were created for the three data sources, namely, the TMPA data with 3-h temporal resolution and 0.25-degree spatial resolution, the TMPA data with 3-h temporal resolution and 0.1-degree spatial resolution, and the

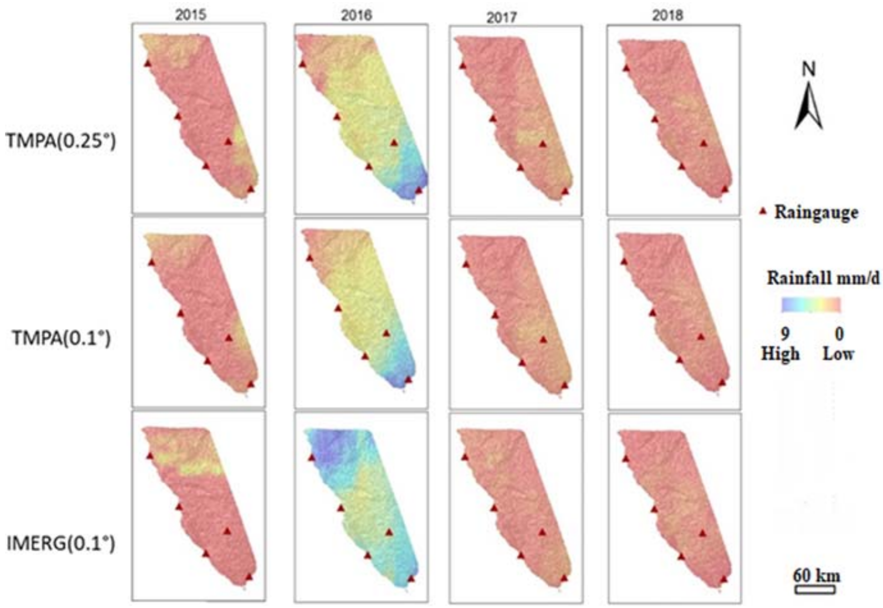

FIGURE 7.3

Spatial distribution of rainfall over the area for each of the four events studied using TMPA and IMERG accumulated scenes (mm day^{-1}). *IMERG*, Integrated Multi-Satellite Retrievals for Global Precipitation Measurement; *TMPA*, Tropical Rainfall Measuring Mission (TRMM) Multisatellite Precipitation Analysis.

IMERG data with half-hour temporal resolution and 0.1-degree spatial resolution. Individual maps were created for all the precipitation events mentioned between 2015 and 2018. The distribution maps illustrate the differences between the three resolution-based datasets. TMPA at 0.25 degrees and 0.1 degrees revealed very similar results. However, noticeable changes were seen between the TMPA datasets and that of the IMERG, especially in the 2016 event, which was the event exhibiting the highest rainfall intensity (see Fig. 7.3).

7.7.4 Statistical metrics

In this section the various statistical metrics that have been utilized in the analysis are outlined.

7.7.4.1 Statistical tests with TMPA and IMERG

Statistical tests were performed with the purpose of evaluating the differences, coherence, and correlation between the TMPA and the IMERG data, both with 0.1-degree spatial resolution. These tests include the Shapiro—Wilk normality test (Shapiro & Wilk, 1965). This test rejects the hypothesis of normality when the respective P-value (denoted by P_{sw}) is less or equal to .05 (i.e., $P_{sw} \leq .05$). The Wilcoxon signed-ranked test (Wilcoxon, 1945) compares two dependent samples to determine if their populations have the same distribution by comparing their medians. The two samples show no differences and considerable dependency when the respective P-value (denoted by P_w) is greater than .05 (i.e., $P_w > .05$). The Spearman correlation coefficient (denoted by R_s) determines the correspondence between two variables. If the two samples exhibit a perfect positive correlation, then $R_s = 1$. For a perfect negative correlation, $R_s = -1$, and for no correlation, $R_s = 0$. The null hypothesis (H_0) that any correlation between the two variables is due to chance is tested by calculating the Spearman test P-value (denoted by P_s). This test examines whether the rankings of each dataset are similar (the relationship does not have to be linear). In this study, for $P_s < .01$, H_0 is very strongly rejected, for $.01 \leq P_s < .05$, H_0 is strongly rejected, for $.05 \leq P_s < .1$, the evidence for rejecting H_0 is weak, and for $P_s \geq .1$, the evidence for rejecting H_0 is very weak.

7.7.4.2 Compatibility of TMPA and IMERG data to rain-gauge measurements

The second group of verification statistics was selected with the purpose of identifying the remote sensing product with higher compatibility with the in situ gauges. A Spearman correlation coefficient test was applied between the rain-gauge data and the TMPA (0.25 degrees), TMPA (0.1 degrees), and IMERG (0.1 degrees) data, which were all collected between 2015 and 2018. This was done to determine the correlation strength between the remote sensing data and the benchmark.

A root mean square error (*RMSE*) test was performed to determine the distribution of the error. A bias test (*Bias%*) was used to evaluate the size of the differences between the two datasets, and a mean absolute error (*MAE*) test corresponds to the mean magnitude of the errors without considering their direction. The mathematical expressions for these statistical metrics are as follows (see Chen et al., 2018; Kim et al., 2017):

$$RMSE = \sqrt{\frac{1}{n}\sum_{i=1}^{n}(P\ sati - P\ gaui)^2} \tag{7.2}$$

$$Bias = \frac{1}{n}\sum_{i=1}^{n}(P\ sati - P\ gaui) \tag{7.3}$$

$$MAE = \frac{1}{n}\sum_{i=1}^{n}\left|P\ sati - P\ gaui\right| \tag{7.4}$$

In the abovementioned expressions, P_{sat} refers to satellite-related precipitation records, P_{gau} represents the records derived from the in situ rain gauges, and n is defined as the number of samples.

7.7.4.3 TMPA and IMERG data in detecting rainfall

The ability of the TMPA and IMERG data to accurately detect rainfall rates at three different threshold values (0.1, 1, and 10 mm) was analyzed. The group of categorical statistics that was used consists of the probability of detection (*POD*), the false alarm ratio (*FAR*), and the Critical Success Index (*CSI*). These were calculated for each single event in an effort to investigate the potential of the satellite products at the abovementioned three rainfall thresholds (Chen et al., 2018; Kim et al., 2017). The three categorical statistics are calculated as functions of Hits, Misses, and False Alarms, as explained in the contingency Table 7.2. The *POD* determines the fraction of the correctly detected precipitation events (Ebert, 2007), the *FAR* provides the fraction of false alarms (Kim et al., 2017), and the *CSI* calculates the correct number of detected events divided by a total number of False alarms, Hits, and Misses. The following are the mathematical expressions for the *POD*, *FAR*, and *CSI*, as they have been used in the analysis:

$$POD = \frac{\text{Hits}}{\text{Hits} + \text{Misses}} \tag{7.5}$$

$$FAR = \frac{\text{False alarms}}{\text{Hits} + \text{False alarms}} \tag{7.6}$$

$$CSI = \frac{\text{Hits}}{\text{Hits} + \text{False alarms} + \text{Misses}} \tag{7.7}$$

7.7.5 Discussion of results

The results of the statistical tests for the TMPA and IMERG datasets are given in Table 7.3. The results of the Shapiro–Wilk normality test have revealed that both datasets are nonnormally distributed, with $P_{sw} < .05$, at all times and for both the *Lowland* and *Highland* regions. This test was essential for determining the subsequent statistical analysis to be applied, as elaborated next. First, given that the data were determined to be nonnormally distributed, the Wilcoxon signed-rank test was applied to elucidate the similarities and differences between the two sets. For the 2015 *Lowland* event, no significant differences between the two datasets were noted at the start of the event but significant differences were noted later. Moreover, the two datasets pertaining to the *Highland* region featured significant differences at alltime thresholds of the precipitation event. For the 2016 event a

Table 7.2 Contingency table for the compatibility between the rain gauges and satellite precipitation products for each precipitation threshold.

	Gauge ≥ threshold	Gauge < threshold
Satellite ≥ threshold	Hits	False alarm
Satellite < threshold	Misses	Correct negatives

Table 7.3 Results of the statistical tests for comparing Tropical Rainfall Measuring Mission (TRMM) Multisatellite Precipitation Analysis and Integrated Multi-Satellite Retrievals for Global Precipitation Measurement data over the *Highland* and *Lowland* regions at successive times of 0, 3, 6, 9, 12, and 24 h from the start of the rainfall event: (1) the Wilcoxon signed-rank tests (P_w, values $P_w < .05$ are denoted as D, indicating a significant difference between the two sets, otherwise they are denoted as ND (no difference), (2) the Spearman correlation coefficient (R_s; negative values indicate a negative correlation), (3) the Spearman P-value range (P_s, where VS (very strong) denotes very strong evidence for rejecting the null hypothesis [$P_s < .01$], S strong evidence [$.01 \leq P_s < .05$], W weak evidence [$.05 \leq P_s < .1$], and VW (very weak) very weak evidence [$P_s \geq 0.1$].

Event	**Region**	**Time (h)**	**Wilcoxon *P*-value P_w**	**Spearman correlation R_s**	**Spearman *P*-value P_s**
2015	*Lowland*	0	ND [0.1873]	−0.16	VW [0.1922]
		3	ND [0.5814]	0.61	VS [8.919×10^{-8}]
		6	D [3.325×10^{-6}]	0.39	VS [0.0015]
		9	D [3.189×10^{-15}]	0.28	S [0.0228]
		12	D [1.62×10^{-15}]	0.43	VS [0.0003]
		24	D [2.894×10^{-16}]	0.46	VS [0.0001]
	Highland	0	D [0.0002]	−0.04	VW [0.6976]
		3	D [0.0002]	−0.03	VW [0.7823]
		6	D [9.49×10^{-14}]	−0.33	VS [0.0003]
		9	D [2.2×10^{-16}]	−0.52	VS [9.125×10^{-10}]
		12	D [2.2×10^{-16}]	−0.44	VS [3.934×10^{-7}]
		24	D [2.2×10^{-16}]	−0.28	VS [0.0018]

(*Continued*)

Table 7.3 Results of the statistical tests for comparing Tropical Rainfall Measuring Mission (TRMM) Multisatellite Precipitation Analysis and Integrated Multi-Satellite Retrievals for Global Precipitation Measurement data over the *Highland* and *Lowland* regions at successive times of 0, 3, 6, 9, 12, and 24 h from the start of the rainfall event: (1) the Wilcoxon signed-rank tests (P_w, values $P_w < .05$ are denoted as D, indicating a significant difference between the two sets, otherwise they are denoted as ND (no difference), (2) the Spearman correlation coefficient (R_s; negative values indicate a negative correlation), (3) the Spearman *P*-value range (P_s, where VS (very strong) denotes very strong evidence for rejecting the null hypothesis [$P_s < .01$], S strong evidence [$.01 \leq P_s < .05$], W weak evidence [$.05 \leq P_s < .1$], and VW (very weak) very weak evidence [$P_s \geq 0.1$].
Continued

Event	Region	Time (h)	Wilcoxon *P*-value P_w	Spearman correlation R_s	Spearman *P*-value P_s
2016	*Lowland*	0	D [1.722×10^{-7}]	0.68	VS [3.609×10^{-10}]
		3	ND [0.0630]	0.44	VS [0.0002]
		6	D [7.602×10^{-6}]	0.03	VW [0.7942]
		9	D [1.763×10^{-12}]	−0.51	VS [1.097×10^{-5}]
		12	D [1.641×10^{-13}]	−0.52	VS [7.236×10^{-6}]
		24	D [1.641×10^{-13}]	−0.52	VS [7.236×10^{-6}]
	Highland	0	D [2.2×10^{-16}]	0.87	VS [2.2×10^{-16}]
		3	ND [0.4478]	0.91	VS [2.2×10^{-16}]
		6	D [1.541×10^{-7}]	0.49	VS [3.234×10^{-8}]
		9	D [2.2×10^{-16}]	−0.14	VW [0.1266]
		12	D [2.2×10^{-16}]	−0.21	S [0.0244]
		24	D [2.2×10^{-16}]	−0.1	S [0.0244]

2017	*Lowland*	0	ND [0.2178]	0.56	VS [1.06×10^{-6}]
		3	D [0.02497	0.38	VS [0.0020]
		6	ND [0.7156]	0.52	VS [8.462×10^{-6}]
		9	ND [0.9647]	−0.27	W [0.0294]
		12	D [0.0004]	0.14	VW [0.2550]
		24	D [2.039×10^{-6}]	0.23	VW [0.0671]
	Highland	0	D [0.0012]	0.15	VW [0.1070]
		3	ND [0.1134]	0.01	VW [0.9563]
		6	D [8.091×10^{-6}]	−0.02	VW [0.8219]
		9	D [0.0001]	−0.55	VS [1.234×10^{-10}]
		12	D [0.0002]	−0.46	VS [1.133×10^{-7}]
		24	ND [0.261]	−0.1	VW [0.2988]
2018	*Lowland*	0	ND [0.0612]	0.42	VS [0.0085]
		3	ND [0.0556]	0.71	VS [0.0002]
		6	D [0.0046]	0.7	VS [5.82×10^{-5}]
		9	ND [0.1368]	0.64	VS [0.0007]
		12	ND [0.1368]	0.64	VS [0.0007]
		24	ND [0.1368]	0.64	VS [0.0007]
	Highland	0	D [2.2×10^{-16}]	0.42	VS [1.776×10^{-6}]
		3	ND [0.7851]	0.71	VS [2.2×10^{-16}]
		6	ND [0.3289]	0.7	VS [2.2×10^{-16}]
		9	D [0.0329]	0.64	VS [2.2×10^{-16}]
		12	D [0.0329]	0.64	VS [2.2×10^{-16}]
		24	D [0.03293]	0.64	VS [2.2×10^{-16}]

large difference was observed between the two datasets, in both the *Lowland* and *Highland* regions at almost all times. For the 2017 event, no significant differences were noted between the *Lowland* datasets at time thresholds 0, 6, and 9 h; significant differences were, however, apparent at the 3, 12, and 24 h time marks. Regarding the *Highland* region, there were significant differences at 0, 6, 9, and 12 h, and no significant differences at 3 and 24 h. The 2018 event featured highly significant differences between the two sets collected over the *Lowland* region at 0, 6, and 9 h. However, no differences were recorded at 3, 12, and 24 h. The *Highland* region is marked with no significant differences between the two datasets at 3 and 6 h but with highly significant differences at 0, 9, 12, and 24 h. Comparing the dataset differences during light-intensity events with those of the moderate-to-heavy-intensity events, it is clear that the data associated with light-intensity events generally feature reduced variability and higher coherence. Comparing data from the *Lowland* and *Highland* regions, there was also a greater uniformity over the *Lowland* region.

Second, the calculations for the Spearman's rank correlation coefficient (R_s) and its associated *P*-value (P_s) revealed a very strong evidence for a positive correlation between the two 2018 satellite-based datasets, at all times and for both the *Lowland* and *Highland* regions (see also Fig. 7.4). However, for the other events, the situation is not straightforward. At the onset of the 2015 event,

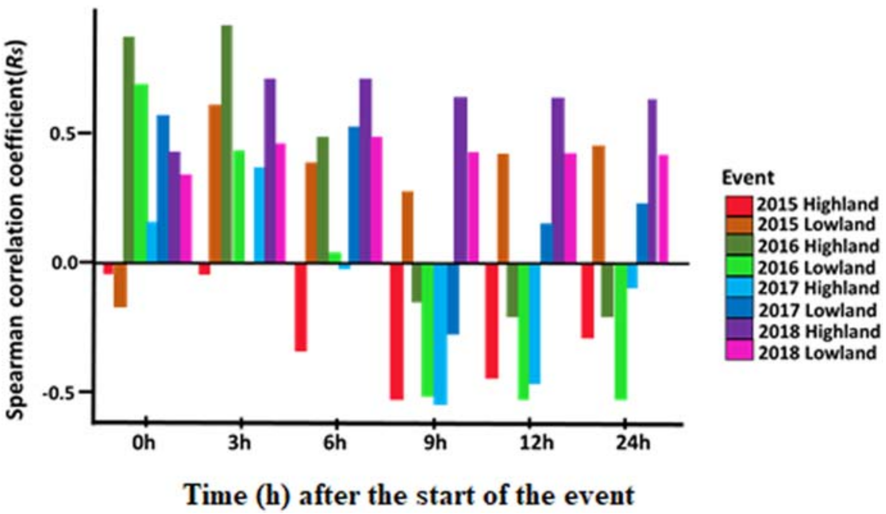

FIGURE 7.4

Bar plot of the Spearman correlation coefficient (R_S) of the two sets of remote sensing data, TMPA and IMERG, over the *Highland* and *Lowland* regions between onset and 24 h. *IMERG*, Integrated Multi-Satellite Retrievals for Global Precipitation Measurement; *TMPA*, Tropical Rainfall Measuring Mission (TRMM) Multisatellite Precipitation Analysis.

a very weak evidence that the data are correlated was observed over the *Lowland* region; however, a strong or very strong evidence of correlation was found for the subsequent time thresholds. Over the *Highland* region, the 2015 satellite-based datasets exhibit a negative R_s at all times, with a very weak evidence for correlation at onset and at 3 h, but with a very strong evidence afterward. For the 2016 event, there is a very strong evidence that the two datasets are correlated except for limited times after the onset of the events. Also, the correlation was found to be negative for all time thresholds from 9 h onward, for both the *Lowland* and *Highland* regions. For the 2017 event the *Lowland* region exhibits evidence for a very strong correlation during the first 6 h of the event that subsequently changes into a weak or very weak; the correlation is positive at almost all times. Regarding the *Highland* region, the situation is generally reversed, with very weak evidence during the first 6 h, subsequently changing into very strong. The correlation coefficient is positive initially, but it turns negative into the later stages of the event.

The Spearman correlation coefficient and the respective P-value were also calculated in an attempt to establish the relationship between the in situ rain gauge records, on the one hand, and the 0.25-degree resolution TMPA data, on the other hand, in this respect, it was found that $R_s = 0.328$ and $P_s = .157$ (see Fig. 7.5). A similar approach was followed in establishing the relationship between the in situ rain- gauge records and the 0.1-degree resolution TMPA, where $R_s = 0.546$ and $P_s = .012$. For the relationship between the in situ rain gauge records and the 0.1-degree resolution IMERG, $R_s = 0.745$ and $P_s = .00016$. Bearing in mind these results, it can be inferred that IMERG exhibited the strongest evidence for correlation with the rain gauges, whereas the 0.25-degree resolution TRMM data the evidence for correlation with the rain gauges was very weak. Moreover, the 0.25- and 0.1-degree spatial resolution TMPA records revealed an underestimation of precipitation during the moderate and heavy-intensity events, while the light event records were highly coherent with the rain gauge records. IMERG displayed this same coherence with the light events, but both underestimated and overestimated values were recorded during the heavy-intensity events.

The RMSE, MAE, and BIAS were calculated for each event and are summarized in Table 7.4 and delineated in Fig. 7.6 as boxplot graphs featuring the maximum and minimum limits, the 25th percentile, the 75th percentile, and the median of each metric. The IMERG dataset displayed the lowest RMSE values for the 2015, 2016, and 2018 precipitation events (10.677, 10.562, and 1.883, respectively). Also, IMERG exhibited the lowest MAE values for 2015, 2016, and 2018 events (6.726, 8.076, and 1.367, respectively). The values from the TMPA 0.1-degree dataset were close to those of the TMPA 0.25-degree dataset, but with better performance. As it should be expected, the lowest bias is related to the coarsest resolution dataset, namely, IMERG. Furthermore, in the BIAS test for the 2015 and 2016 events, IMERG exhibited values closest to 0.

The third group of categorical statistics was applied to the three different precipitation thresholds: 0.1, 1, and 10 mm. The results, shown in Fig. 7.7, illustrate

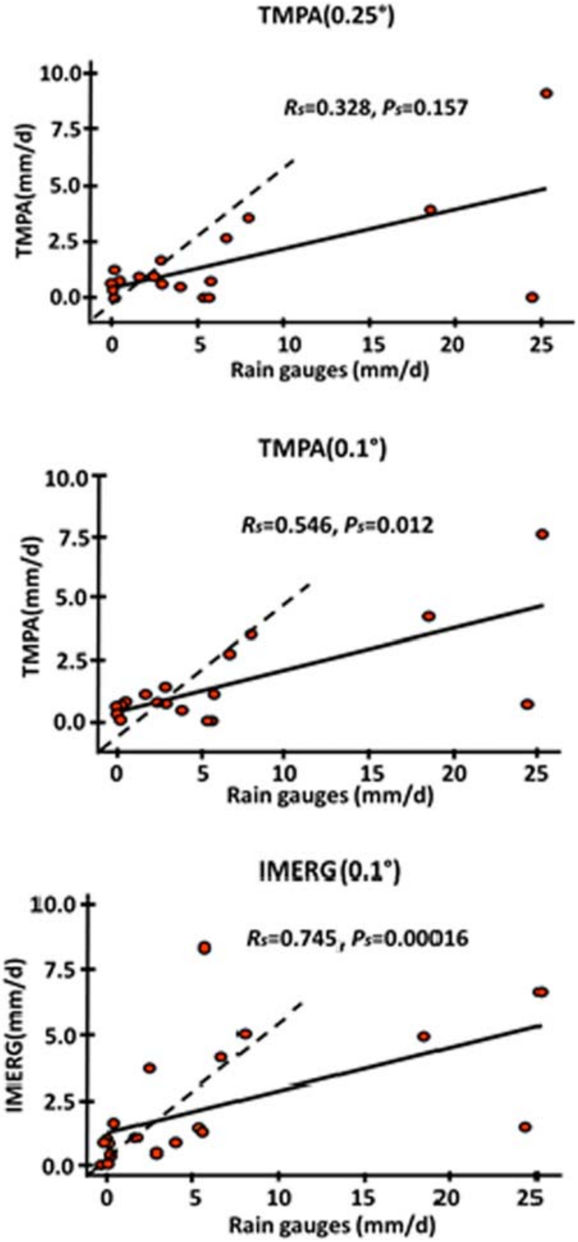

FIGURE 7.5

Spearman correlation (R_S) and P-value (P_S) between remote sensing data, at spatial resolutions of TMPA 0.25 degrees (top), TMPA 0.1 degrees (middle), and IMERG 0.1 degrees (bottom) and rain gauge records. The solid line represents the fitted linear regression. *IMERG*, Integrated Multi-Satellite Retrievals for Global Precipitation Measurement; *TMPA*, Tropical Rainfall Measuring Mission (TRMM) Multisatellite Precipitation Analysis.

Table 7.4 Root mean square error (RMSE), mean absolute error (MAE), and bias (BIAS) for each recorded event with spatial resolutions specified.

Event (product)	Metric RMSE	MAE	BIAS
2015 (TMPA 0.25°)	11.51	7.45	0.63
2015 (TMPA 0.1°)	11.23	7.35	0.64
2015 (IMERG 0.1°)	10.67	6.72	0
2016 (TMPA 0.25°)	10.43	8.93	0.69
2016 (TMPA 0.1°)	10.72	9.03	0.68
2016 (IMERG 0.1°)	10.56	8.07	0.36
2017 (TMPA 0.25°)	0.82	0.72	−1.62
2017 (TMPA 0.1°)	0.76	0.57	−0.81
2017 (IMERG 0.1°)	1.2	0.89	−1.71
2018 (TMPA 0.25°)	1.94	1.47	0.96
2018 (TMPA 0.1°)	1.91	1.37	1.01
2018 (IMERG 0.1°)	1.88	1.36	1.01

IMERG, *Integrated Multi-Satellite Retrievals for Global Precipitation Measurement;* TMPA, *Tropical Rainfall Measuring Mission (TRMM) Multisatellite Precipitation Analysis.*

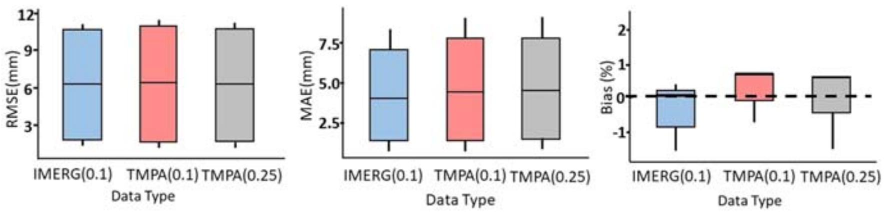

FIGURE 7.6

Boxplots of RMSE, BIAS%, and MAE values recorded by every single event. *MAE*, Mean absolute error; *RMSE*, mean square error.

the high capability of the TMPA and IMERG analyses in detecting light-intensity events, as the 0.1-mm threshold performed best with both types of remote sensing data, calculating a 1 in the POD and CSI tests, and 0.4 and 0.2 in the FAR test. The second threshold also results in a 1 in the POD test for both datasets, but the CSI calculates at 0.8 and 1, and the FAR test results in 0.4 and 0.5. The highest threshold, 10 mm, produces the worst results. TMPA amounts to a 0 on all the aforementioned tests. IMERG records a 1, 1, and 0.3 for the POD, FAR, and CSI, respectively. In general, the IMERG data show better results than that of the TMPA. Both datasets feature higher certainty for light-intensity events.

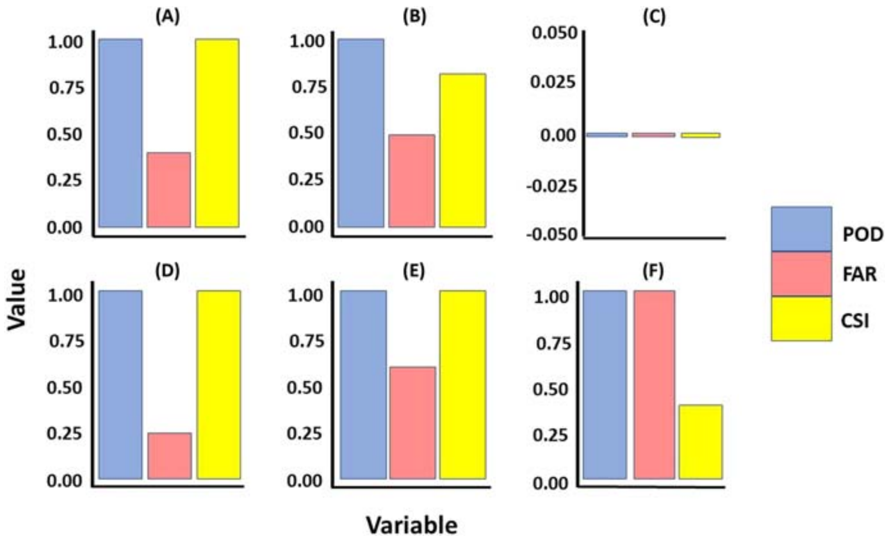

FIGURE 7.7

Bar plots of POD, FAR, and CSI results of the TMPA and IMERG for three different thresholds (0.1, 1, and 10 mm) using data from all events. Parts (A), (B), and (C) represent the 0.1-, 1-, and 10-mm thresholds for the TMPA data, respectively; parts (D), (E), and (F) represent the 0.1-, 1-, and 10-mm thresholds for the IMERG data. *CSI*, Critical Success Index; *FAR*, false alarm ratio; *IMERG*, Integrated Multi-Satellite Retrievals for Global Precipitation Measurement; *POD*, probability of detection; *TMPA*, Tropical Rainfall Measuring Mission (TRMM) Multisatellite Precipitation Analysis.

7.8 Concluding remarks

With an increasing spatiotemporal resolution of the satellite-related rainfall datasets, more emphasis is given worldwide in using these sources of rainfall analyses in a wide range of applications. Two such datasets have been utilized in the present study, TMPA and IMERG. These datasets were compared between them and against a local rain gauge network in El-Qaa Plain, Sinai Peninsula.

The statistical metrics are used to demonstrate the low correlation and significant differences between the pixel values of the TMPA and IMERG datasets in the moderate and heavy intensity 2015 and 2016 events; datasets from the light-intensity events, namely, 2017 and 2018, were more highly correlated. Additionally, the values recorded over the *Lowland* region were more uniform than those of the *Highland* region, where a greater variation was observed.

When the two satellite-related rainfall datasets were compared to the rain-gauge data, it was noted that their performance was best during the light-intensity events, particularly around the event onset (3 and 6 h). In contrast, poorer performance was noted during intense events and at the later precipitation stages in such events (12 and 24 h). Data coherence and uniformity were lower in the *Highland* region when compared to the *Lowland* region data. TMPA and IMERG were compared to the limited rain-gauge records, using various statistical metrics to evaluate their effectiveness in replicating in situ observations. Performance varied, with the IMERG data demonstrating the best performance, producing the lowest *RMSE*, *BIAS*, and *MAE* values. This was followed by the 0.1-degree resolution TMPA and the 0.25-degree resolution TMPA data, with the latter exhibiting the weakest performance.

Categorical statistics have indicated high performance by both the TMPA and IMERG, during the light-intensity events. However, low certainty was observed for the high-intensity events. Overall, the IMERG dataset performed better than the TMPA in all thresholds. The findings of this study could be used to support the postulation on the superior performance of IMERG over TMPA in arid and semiarid areas, but this cannot be generalized. Despite the general superior performance of the IMERG dataset, lack of sufficient data over the mountainous region as well as heavy-intensity precipitation events, indicating that it would not be used as a substitute for rain-gauge data. However, it can be used as a promising alternative for rain-gauge records during the relatively frequent light-intensity events until a new rain-gauge network is in place, optimized, and implemented. Even when such an upgraded network is put into operation, IMERG can continue to supplement the in situ data, either for monitoring purposes or for filling in the gaps in the network.

Any alternative or complementary rainfall estimating systems (i.e., satellite-related) adopted in arid and semiarid environments receive most of their precipitation during cases with small amounts of rainfall. The skill of such a system to estimate precipitation adequately during such events is very important. Due to the limited amount of in situ data, the effect of elevation on the estimation of rainfall from satellite-derived products cannot be done in a satisfactory way in the present study. This is a very challenging viewpoint that has been pursued in other studies with more ground-based data (e.g., Retalis et al., 2020).

The inconsistencies between the satellite-derived products and the in situ measurements underline the necessity for improving future versions of IMERG algorithms, by taking into account the variations in meteorology and geography, especially in semiarid areas of the globe. The need is for more efficient physically based algorithms, based on a comparison with surface observations across all major precipitating synoptic conditions.

Acknowledgments

The Helmholtz Center for Environmental Research in Leipzig, Germany, Tübingen University in Germany, and Suez Canal University in Egypt funded the research reported in this chapter. The NASA/Goddard Space Flight Center’s Mesoscale Atmospheric Processes Laboratory and Precipitation Processing Center, which produced and computed the TMPA and IMERG data, is acknowledged by the authors.

References

Abera, W., Brocca, L., & Rigon, R. (2016). Comparative evaluation of different satellite rainfall estimation products and bias correction in the Upper Blue Nile (UBN) basin. *Atmospheric Research*, *178–179*, 471–483. Available from https://doi.org/10.1016/j.atmosres.2016.04.017.

Abuzied, S., Yuan, M., Ibrahim, S., Kaiser, M., & Saleem, T. (2016). Geospatial risk assessment of flash floods in Nuweibaa area, Egypt. *Journal of Arid Environments*, *133*, 54–72. Available from https://doi.org/10.1016/j.jaridenv.2016.06.004.

Adler, R. F., Huffman, G. J., Chang, A., Ferraro, R., Xie, P. P., Janowiak, J., Rudolf, B., Schneider, U., Curtis, S., Bolvin, D., Gruber, A., Susskind, J., Arkin, P., & Nelkin, E. (2003). The version-2 global precipitation climatology project (GPCP) monthly precipitation analysis (1979–present). *Journal of Hydrometeorology*, *4*(6), 1147–1167, https://doi.org/10.1175/1525-7541(2003)004 < 1147:TVGPCP > 2.0.CO;2.

Adler, R. F., Sapiano, M. R. P., Huffman, G. J., Wang, J.-J., Gu, G., Bolvin, D., Chiu, L., Schneider, U., Becker, A., Nelkin, E., Xie, P., Ferraro, R., & Shin, D.-B. (2018). The global precipitation climatology project (GPCP) monthly analysis (new version 2.3) and a review of 2017 global precipitation. *Atmosphere*, *9*(4). Available from https://doi.org/10.3390/atmos9040138.

Ahmed, M., Sauck, W., Sultan, M., Yan, E., Soliman, F., & Rashed, M. (2014). Geophysical constraints on the hydrogeologic and structural settings of the gulf of Suez Rift-related basins: Case study from the El Qaa Plain, Sinai, Egypt. *Surveys in Geophysics*, *35*(2), 415–430. Available from https://doi.org/10.1007/s10712-013-9259-6.

Alemohammad, S. H., Entekhabi, D., & Mclaughlin, D. B. (2014). Evaluation of long-term SSM/I-based precipitation records over land. *Journal of Hydrometeorology*, *15*(5), 2012–2029. Available from https://doi.org/10.1175/JHM-D-13-0171.1.

Anjum, M. N., Ahmad, I., Ding, Y., Shangguan, D., Zaman, M., Ijaz, M. W., Sarwar, K., Han, H., & Yang, M. (2019). Assessment of IMERG-V06 precipitation product over different hydro-climatic regimes in the Tianshan mountains. *Remote Sensing*, *11*, 2314. Available from https://doi.org/10.3390/rs11192314.

Anjum, M. N., Ding, Y., Shangguan, D., Ahmad, I., Ijaz, M. W., Farid, H. U., Yagoub, Y. E., Zaman, M., & Adnan, M. (2018). Performance evaluation of latest integrated multi-satellite retrievals for Global Precipitation Measurement (IMERG) over the northern highlands of Pakistan. *Atmospheric Research*, *205*, 134–146. Available from https://doi.org/10.1016/j.atmosres.2018.02.010.

Ashouri, H., Hsu, K. L., Sorooshian, S., Braithwaite, D. K., Knapp, K. R., Cecil, L. D., Nelson, B. R., & Prat, O. P. (2015). PERSIANN-CDR: Daily precipitation climate data record from multisatellite observations for hydrological and climate studies. *Bulletin of the American Meteorological Society*, *96*(1), 69–83. Available from https://doi.org/10.1175/BAMS-D-13-00068.1.

Azab, A. A., & El-Khadragy, A. A. (2013). 2.5-D Gravity/magnetic model studies in Sahl El Qaa Area, southwestern Sinai, Egypt. *Pure and Applied Geophysics*, *170*(12), 2207–2229. Available from https://doi.org/10.1007/s00024-013-0650-5.

Beck, H. E., Van Dijk, A. I. J. M., Levizzani, V., Schellekens, J., Miralles, D. G., Martens, B., & De Roo, A. (2017). MSWEP: 3-hourly 0.25° global gridded precipitation (1979–2015) by merging gauge, satellite, and reanalysis data. *Hydrology and Earth System Sciences*, *21*(1), 589–615. Available from https://doi.org/10.5194/hess-21-589-2017.

Berg, W., Sapiano, M. R., Horsman, J., & Kummerow, C. (2012). Improved geolocation and Earth incidence angle information for a fundamental climate data record of the SSM/I sensors. *IEEE Transactions on Geoscience and Remote Sensing*, *51*(3), 1504–1513. Available from https://doi.org/10.1109/tgrs.2012.2199761.

Beven, K. (2004). Robert E. Horton's perceptual model of infiltration processes. *Hydrological Processes*, *18*(17), 3447–3460. Available from https://doi.org/10.1002/hyp.5740.

Bo, X., Qing-Hai, W., Jun, F., Feng-Peng, H., & Quan-Hou, D. (2011). Application of the SCS-CN Model to runoff estimation in a small watershed with high spatial heterogeneity. *Pedosphere*, *21*, 738–749. Available from https://doi.org/10.1016/s1002-0160(11)60177-x.

Cao, Q., Hao, Z., Zhou, J., Wang, W., Yuan, F., Zhu, W., & Yu, C. (2019). Impacts of various types of El Niño–Southern Oscillation (ENSO) and ENSO Modoki on the rainy season over the Huaihe River basin. *International Journal of Climatology*, *39*(5), 2811–2824. Available from https://doi.org/10.1002/joc.6002.

Chen, C., Chen, Q., Duan, Z., Zhang, J., Mo, K., Li, Z., & Tang, G. (2018). Multiscale comparative evaluation of the GPM IMERG v5 and TRMM 3B42 v7 precipitation products from 2015 to 2017 over a climate transition area of China. *Remote Sensing*, *10*(6). Available from https://doi.org/10.3390/rs10060944.

Crow, W. T., Berg, A. A., Cosh, M. H., Loew, A., Mohanty, B. P., Panciera, R., De Rosnay, P., Ryu, D., & Walker, J. P. (2012). Upscaling sparse ground-based soil moisture observations for the validation of coarse-resolution satellite soil moisture products. *Reviews of Geophysics*, *50*(2). Available from https://doi.org/10.1029/2011RG000372.

Das, R. K., & Prakash, N. R. (2011). Design of an improvised tipping bucket rain gauge for measurement of rain and snow precipitation. *International Journal of Instrumentation Technology*, *1*(1), 44–59. Available from https://doi.org/10.1504/ijit.2011.043597.

Dregne, H., Kassas, M., & Rosanov, B. (1991). A new assessment of the world status of desertification. *Desertification Control Bulletin*, *20*, 6–29. Available from https://wedocs.unep.org/handle/20.500.11822/28989.

Dyck, S., Grünewald, U., Kluge, C., Schramm, M., & Lauterbach, D. (1980). *Angewandte hydrologie: Teil 1: Berechnung und Regelung des Durchflusses der Flüsse* (2nd ed.). Ernst & Sohn.

Ebert, E.E. (2007). Methods for verifying satellite precipitation estimates. In: Measuring precipitation from space, EURAINSAT and the future. Levizzani, V., Bauer, P., Turk, F. J. (Eds.), Springer, 345–356.

Eissa, M. A., Mahmoud, H. H., Shouakar-Stash, O., El-Shiekh, A., & Parker, B. (2016). Geophysical and geochemical studies to delineate seawater intrusion in Bagoush area, northwestern coast, Egypt. *Journal of African Earth Sciences*, *121*, 365–381. Available from https://doi.org/10.1016/j.jafrearsci.2016.05.031.

El-Fakharany, M. A. (2016). Geophysical and hydrogeochemical investigations of the Quaternary aquifer at the middle part of El Qaa Plain SW Sinai, Egypt. *Egyptian Journal of Geology*, *47/2*.

El-Refai, A. A. (1992). Water resources of southern Sinai, Egypt. (Geomorphological and Hydrogeological studies) (PhD thesis). Faculty of Science, University of Cairo, Egypt.

Ezzahar, J., Chehbouni, A., Hoedjes, J. C. B., Er-Raki, S., Chehbouni, A., Boulet, G., Bonnefond, J. M., & De Bruin, H. A. R. (2007). The use of the scintillation technique for monitoring seasonal water consumption of olive orchards in a semi-arid region. *Agricultural Water Management*, *89*(3), 173–184. Available from https://doi.org/10.1016/j.agwat.2006.12.015.

Fang, J., Yang, W., Luan, Y., Du, J., Lin, A., & Zhao, L. (2019). Evaluation of the TRMM 3B42 and GPM IMERG products for extreme precipitation analysis over China. *Atmospheric Research*, *223*, 24–38. Available from https://doi.org/10.1016/j.atmosres.2019.03.001.

Fensterseifer, C., Allasia, D. G., & Paz, A. R. (2016). Assessment of the TRMM 3B42 precipitation product in southern Brazil. *Journal of the American Water Resources Association*, *52*(2), 367–375. Available from https://doi.org/10.1111/1752-1688.12398.

Ghodeif, K., & Gorski, J. (2001). Protection of fresh ground water in El-Qaa Quaternary aquifer. In *New approaches characterizing groundwater flow* (pp. 71–76).

Guo, H., Bao, A., Ndayisaba, F., Liu, T., Kurban, A., & De Maeyer, P. (2017). Systematical evaluation of satellite precipitation estimates over Central Asia using an improved error-component procedure. *Journal of Geophysical Research: Atmospheres*, *122*(20), 10–927. Available from https://doi.org/10.1002/2017JD026877.

Guo, H., Chen, S., Bao, A., Behrangi, A., Hong, Y., Ndayisaba, F., Hu, J., & Stepanian, P. M. (2016). Early assessment of Integrated multi-satellite retrievals for global precipitation measurement over China. *Atmospheric Research*, *176–177*, 121–133. Available from https://doi.org/10.1016/j.atmosres.2016.02.020.

Han, S. C., Yeo, I. Y., Alsdorf, D., Bates, P., Boy, J. P., Kim, H., Oki, T., & Rodell, M. (2010). Movement of Amazon surface water from time-variable satellite gravity measurements and implications for water cycle parameters in land surface models. *Geochemistry, Geophysics, Geosystems*, *11*(9). Available from https://doi.org/10.1029/2010GC003214.

Hartmann, H. C., Pagano, T. C., Sorooshian, S., & Bales, R. (2002). Confidence builders: Evaluating seasonal climate forecasts from user perspectives. *Bulletin of the American Meteorological Society*, *83*(5), 683–698, https://doi.org/10.1175/1520-0477(2002)083 < 0683:CBESCF > 2.3.CO;2.

Heath, R. C. (1983). *Basic ground-water hydrology: United States geological survey water-supply paper 2220. United States Geological Survey*.

Horton, R. E. (1941). An approach toward a physical interpretation of infiltration-capacity 1. *Soil Science Society of America Journal*, *5*(C), 399–417.

Hou, A. Y., Kakar, R. K., Neeck, S., Azarbarzin, A. A., Kummerow, C. D., Kojima, M., Oki, R., Nakamura, K., & Iguchi, T. (2014). The global precipitation measurement mission. *Bulletin of the American Meteorological Society*, *95*(5), 701–722. Available from https://doi.org/10.1175/BAMS-D-13-00164.1.

Hou, A. Y., Skofronick-Jackson, G., Kummerow, C. D., & Shepherd, J. M. (2008). *Global precipitation measurement*. *Precipitation: Advances in measurement, estimation and prediction* (pp. 131–169). Berlin Heidelberg: Springer. Available from https://doi.org/10.1007/978-3-540-77655-0_6.

Huffman, G. J., Adler, R. F., Bolvin, D. T., Gu, G., Nelkin, E. J., Bowman, K. P., Hong, Y., Stocker, E. F., & Wolff, D. B. (2007). The TRMM multisatellite precipitation analysis (TMPA): Quasi-global, multiyear, combined-sensor precipitation estimates at fine scales. *Journal of Hydrometeorology*, *8*(1), 38–55. Available from https://doi.org/10.1175/JHM560.1.

Huffman, G. J., Adler, R. F., Bolvin, D. T., & Nelkin, E. J. (2010). *The TRMM multi-satellite precipitation analysis (TMPA). Satellite rainfall applications for surface* *hydrology* (pp. 3–22). Netherlands: Springer. Available from https://doi.org/10.1007/978-90-481-2915-7_1.

Huffman, G. J., Bolvin, D. T., Braithwaite, D., Hsu, K. L., Joyce, R. J., Kidd, C., Nelkin, E. J., Sorooshian, S., Stocker, E. F., Tan, J., Wolff, D. B., & Xie, P. (2020). *Integrated multi-satellite retrievals for the global precipitation measurement (GPM) mission (IMERG)*, . *Advances in global change research* (Vol. 67, pp. 343–353). Springer. Available from https://doi.org/10.1007/978-3-030-24568-9_19.

Immerzeel, W. W., Rutten, M. M., & Droogers, P. (2009). Spatial downscaling of TRMM precipitation using vegetative response on the Iberian Peninsula. *Remote Sensing of Environment*, *113*(2), 362–370. Available from https://doi.org/10.1016/j.rse.2008.10.004.

Joyce, R. J., Janowiak, J. E., Arkin, P. A., & Xie, P. (2004). CMORPH: A method that produces global precipitation estimates from passive microwave and infrared data at high spatial and temporal resolution. *Journal of Hydrometeorology*, *5*(3), 487–503, https://doi.org/10.1175/1525-7541(2004)005 < 0487:CAMTPG > 2.0.CO;2.

Joyce, R. J., Xie, P., Yarosh, Y., Janowiak, J. E., & Arkin, P. A. (2010). *CMORPH: A morphing approach for high resolution precipitation product generation*. *Satellite rainfall applications for surface hydrology* (pp. 23–37). Netherlands: Springer. Available from https://doi.org/10.1007/978-90-481-2915-7_2.

Kalma, J. D., McVicar, T. R., & McCabe, M. F. (2008). Estimating land surface evaporation: A review of methods using remotely sensed surface temperature data. *Surveys in Geophysics*, *29*(4–5), 421–469. Available from https://doi.org/10.1007/s10712-008-9037-z.

Khan, A., Chatterjee, S., Bisai, D., & Barman, N. K. (2014). Analysis of change point in surface temperature time series 585 using cumulative sum chart and bootstrapping for Asansol weather observation station, West Bengal, 586 India. *American Journal of Climate Change*, *3*, 83–94. Available from https://doi.org/10.4236/ajcc.2014.31008.

Kidd, C., & Levizzani, V. (2011). Status of satellite precipitation retrievals. *Hydrology and Earth System Sciences*, *15*(4), 1109–1116. Available from https://doi.org/10.5194/hess-15-1109-2011.

Kim, K., Park, J., Baik, J., & Choi, M. (2017). Evaluation of topographical and seasonal feature using GPM IMERG and TRMM 3B42 over Far-East Asia. *Atmospheric Research*, *187*, 95–105. Available from https://doi.org/10.1016/j.atmosres.2016.12.007.

Kuchment, L. S. (2004). The hydrological cycle and human impact on it. In *Water resources management*.

Kummerow, C., Barnes, W., Kozu, T., Shiue, J., & Simpson, J. (1998). The tropical rainfall measuring mission (TRMM) sensor package. *Journal of Atmospheric and Oceanic Technology*, *15*(3), 809–817, https://doi.org/10.1175/1520-0426(1998)015 < 0809:TTRMMT > 2.0.CO;2.

Kustas, W. P., & Norman, J. M. (1996). Utilisation de la télédétection pour le suivi de l'évapotranspiration sur les terres. *Hydrological Sciences Journal*, *41*(4), 495–516. Available from https://doi.org/10.1080/02626669609491522.

Li, C., Sinha, E., Horton, D. E., Diffenbaugh, N. S., & Michalak, A. M. (2014). Joint bias correction of temperature and precipitation in climate model simulations. *Journal of Geophysical Research*, *119*(23), 13–162. Available from https://doi.org/10.1002/2014JD022514.

Libertino, A., Sharma, A., Lakshmi, V., & Claps, P. (2016). A global assessment of the timing of extreme rainfall from TRMM and GPM for improving hydrologic design. *Environmental Research Letters*, *11*(5). Available from https://doi.org/10.1088/1748-9326/11/5/054003.

Liu, Y. Y., Dorigo, W. A., Parinussa, R. M., De Jeu, R. A. M., Wagner, W., McCabe, M. F., Evans, J. P., & Van Dijk, A. I. J. M. (2012). Trend-preserving blending of passive and active microwave soil moisture retrievals. *Remote Sensing of Environment*, *123*, 280−297. Available from https://doi.org/10.1016/j.rse.2012.03.014.

Lonfat, M. (2004). Tropical cyclone rainfall: An observational and numerical study of the structure and governing physical processes (PhD dissertation). University of Miami, USA, ProQuest Dissertations Publishing.

Long, Y., Zhang, Y., & Ma, Q. (2016). A merging framework for rainfall estimation at high spatiotemporal resolution for distributed hydrological modeling in a data-scarce area. *Remote Sensing*, *8*(7), 599. Available from https://doi.org/10.3390/rs8070599.

Maidment, R. I., Grimes, D., Allan, R. P., Tarnavsky, E., Stringer, M., Hewison, T., Roebeling, R., & Black, E. (2014). The 30-year TAMSAT African rainfall climatology and time-series (TARCAT) dataset. *Journal of Geophysical Research: Atmospheres*, *18*, 10619−10644. Available from https://doi.org/10.1002/2014jd021927.

Maidment, R. I., Grimes, D., Black, E., Tarnavsky, E., Young, M., Greatrex, H., Allan, R. P., Stein, T., Nkonde, E., Senkunda, S., & Alcántara, E. M. U. (2017). A new, long-term daily satellite-based rainfall dataset for operational monitoring in Africa. *Scientific Data*, *4*. Available from https://doi.org/10.1038/sdata.2017.63.

Malagnoux, M. (2007). Arid land forests of the world: global environmental perspectives. In *International conference on afforestation and sustainable forests as a means to combat desertification*. Jerusalem, Israel, 16−19.

Manz, B., Páez-Bimos, S., Horna, N., Buytaert, W., Ochoa-Tocachi, B., Lavado-Casimiro, W., & Willems, B. (2017). Comparative ground validation of IMERG and TMPA at variable spatiotemporal scales in the tropical Andes. *Journal of Hydrometeorology*, *18*(9), 2469−2489. Available from https://doi.org/10.1175/JHM-D-16-0277.1.

Marchok, T., Rogers, R., & Tuleya, R. (2007). Validation schemes for tropical cyclone quantitative precipitation forecasts: Evaluation of operational models for United States landfalling cases. *Weather and Forecasting*, *22*(4), 726−746. Available from https://doi.org/10.1175/WAF1024.1.

Massoud, U., Santos, F., El Qady, G., Atya, M., & Soliman, M. (2010). Identification of the shallow subsurface succession and investigation of the seawater invasion to the Quaternary aquifer at the northern part of El Qaa plain, Southern Sinai, Egypt by transient electromagnetic data. *Geophysical Prospecting*, *58*(2), 267−277. Available from https://doi.org/10.1111/j.1365-2478.2009.00804.x.

McClay, K. R., Nichols, G. J., Khalil, S. M., Darwish, M., & Bosworth, W. (1998). Extensional tectonics and sedimentation, eastern Gulf of Suez, Egypt. In B. H. Purser, & D. W. J. Bosence (Eds.), *Sedimentation and tectonics in Rift Basins Red Sea: Gulf of Aden* (pp. 223−238). Springer. Available from https://doi.org/10.1007/978-94-011-4930-3_14.

Michaelides, S., Levizzani, V., Anagnostou, E., Bauer, P., Kasparis, T., & Lane, J. E. (2009). Precipitation: Measurement, remote sensing, climatology and modeling. *Atmospheric Research*, *94*(4), 512−533. Available from https://doi.org/10.1016/j.atmosres.2009.08.017.

Morsy, M., Scholten, T., Michaelides, S., Borg, E., Sherief, Y., & Dietrich, P. (2021). Comparative analysis of TMPA and IMERG precipitation datasets in the arid environment of El-Qaa Plain, Sinai. *Remote sensing*, *13*(4). Available from https://doi.org/10.3390/rs13040588.

Niu, G. Y., Yang, Z. L., Dickinson, R. E., Gulden, L. E., & Su, H. (2007). Development of a simple groundwater model for use in climate models and evaluation with Gravity Recovery and Climate Experiment data. *Journal of Geophysical Research Atmospheres*, *112*(7). Available from https://doi.org/10.1029/2006JD007522.

Pagano, T., & Sorooshian, S. (2002). Hydrologic cycle. In M. C. MacCracken, & J. S. Perry (Eds.), *Encyclopedia of global environmental change* (Vol. 1). Wiley.

Palomino-Ángel, S., Anaya-Acevedo, J. A., & Botero, B. A. (2019). Evaluation of 3B42V7 and IMERG daily-precipitation products for a very high-precipitation region in northwestern South America. *Atmospheric Research*, *217*, 37−48. Available from https://doi.org/10.1016/j.atmosres.2018.10.012.

Parinussa, R., Wang, G., Liu, Y., Hagan, D., Lin, F., van der Schalie, R., & de Jeu, A. M. (2017). The evaluation of single-sensor surface soil moisture anomalies over the Mainland of the People's Republic of China. *Remote Sensing*, *9*, 149. Available from https://doi.org/10.3390/rs9020149.

Pilgrim, D. H., Chapman, T. G., & Doran, D. G. (1988). Problèmes de la mise au point de modèles pluie-écoulement dans les régions arides et semi-arides. *Hydrological Sciences Journal*, *33*(4), 379−400. Available from https://doi.org/10.1080/02626668809491261.

Pitman, A. J. (2003). The evolution of, and revolution in, land surface schemes designed for climate models. *International Journal of Climatology*, *23*(5), 479−510. Available from https://doi.org/10.1002/joc.893.

Poméon, T., Diekkrüger, B., & Kumar, R. (2018). Computationally efficient multivariate calibration and validation of a grid-based hydrologic model in sparsely gauged West African river basins. *Water (Switzerland)*, *10*(10). Available from https://doi.org/10.3390/w10101418.

Prasad, M. (2002). Acoustic measurements in unconsolidated sands at low effective pressure and overpressure detection. *Geophysics*, *67*(2), 405−412. Available from https://doi.org/10.1190/1.1468600.

Prigent, C. (2010). Precipitation retrieval from space: An overview. *Comptes Rendus—Geoscience*, *342*(4−5), 380−389. Available from https://doi.org/10.1016/j.crte.2010.01.004.

Rashed, M., Sauck, W., & Soliman, F. (2007). Gravity, magnetic, and geoelectric survey on El-Qaa plain, southwest Sinai, Egypt. In *Proceedings of the 8th conference geology of Sinai for development, Ismailia 3 December 2007* (pp. 15−20).

Retalis, A., Katsanos, D., Tymvios, F., & Michaelides, S. (2018). Validation of the first years of GPM operation over Cyprus. *Remote Sensing*, *10*(10). Available from https://doi.org/10.3390/rs10101520.

Retalis, A., Katsanos, D., Tymvios, F., & Michaelides, S. (2020). Comparison of GPM IMERG and TRMM 3B43 products over Cyprus. *Remote Sensing*, *12*(19). Available from https://doi.org/10.3390/rs12193212.

Said, R. (1960). *The geology of Egypt*. Routledge. Available from https://doi.org/10.1201/9780203736678.

Sauck., Kehew, A., Soliman, F., Smart, L., & Mesbah, M. (2005). Basin definition with gravity and resistivity (VES) in the central El Qaa Plain. *Geophysical Research Abstracts*, *7*. Available from https://www.cosis.net/abstracts/EGU05/00066/EGU05-J-00066.pdf.

Sayed, M. A. A., El-Fakharany, M. A., & Hamed, M. F. (2004). Integrated geophysical and hydrogeological studies on the quaternary aquifer at the middle part of El-Qaa Plain. *Journal of Egyptian Geophysical Society*, *2*(1), 135−145.

Scanlon, B. R., Keese, K. E., Flint, A. L., Flint, L. E., Gaye, C. B., Edmunds, W. M., & Simmers, I. (2006). Global synthesis of groundwater recharge in semiarid and arid regions. *Hydrological Processes*, *20*(15), 3335−3370. Available from https://doi.org/10.1002/hyp.6335.

Shapiro, S. S., & Wilk, M. B. (1965). An analysis of variance test for normality (complete samples). *Biometrika*, *52*, 591−611. Available from https://doi.org/10.1093/biomet/52.3-4.591.

Sheffield, J., Wood, E. F., Pan, M., Beck, H., Coccia, G., Serrat-Capdevila, A., & Verbist, K. (2018). Satellite remote sensing for water resources management: Potential for supporting sustainable development in data-poor regions. *Water Resources Research*, *54*(12), 9724−9758. Available from https://doi.org/10.1029/2017WR022437.

Shen, Y., & Chen, Y. (2010). Global perspective on hydrology, water balance, and water resources management in arid basins. *Hydrological Processes*, *24*(2), 129−135. Available from https://doi.org/10.1002/hyp.7428.

Sherief, Y. (2008). Flash floods and their effects on the development in El-Qaá plain area in south Sinai, Egypt, a study in applied geomorphology using GIS and remote sensing (PhD dissertation). Mainz University, Germany. https://www.researchgate.net/publication/288824881

Sorooshian, S., Hsu, K. L., Gao, X., Gupta, H. V., Imam, B., & Braithwaite, D. (2000). Evaluation of PERSIANN system satellite-based estimates of tropical rainfall. *Bulletin of the American Meteorological Society*, *81*(9), 2035−2046, https://doi.org/10.1175/1520-0477(2000)081 < 2035:EOPSSE > 2.3.CO;2.

Sultan, M., Metwally, S., Milewski, A., Becker, D., Ahmed, M., Sauck, W., Soliman, F., Sturchio, N., Yan, E., Rashed, M., Wagdy, A., Becker, R., & Welton, B. (2011). Modern recharge to fossil aquifers: Geochemical, geophysical, and modeling constraints. *Journal of Hydrology*, *403*(1−2), 14−24. Available from https://doi.org/10.1016/j.jhydrol.2011.03.036.

Sun, Q., Miao, C., Duan, Q., Ashouri, H., Sorooshian, S., & Hsu, K. L. (2018). A review of global precipitation data sets: Data sources, estimation, and intercomparisons. *Reviews of Geophysics*, *56*(1), 79−107. Available from https://doi.org/10.1002/2017RG000574.

Tan, M. L., & Duan, Z. (2017). Assessment of GPM and TRMM precipitation products over Singapore. *Remote Sensing*, *9*(7). Available from https://doi.org/10.3390/rs9070720.

Tan, M. L., & Santo, H. (2018). Comparison of GPM IMERG, TMPA 3B42 and PERSIANN-CDR satellite precipitation products over Malaysia. *Atmospheric Research*, *202*, 63−76. Available from https://doi.org/10.1016/j.atmosres.2017.11.006.

Tapiador, F. J., Turk, F. J., Petersen, W., Hou, A. Y., García-Ortega, E., Machado, L. A. T., Angelis, C. F., Salio, P., Kidd, C., Huffman, G. J., & de Castro, M. (2012). Global precipitation measurement: Methods, datasets, and applications. *Atmospheric Research*, *104−105*, 70−97. Available from https://doi.org/10.1016/j.atmosres.2011.10.021.

Thornes, J. B. (2009). *Catchment and channel hydrology*. *Geomorphology of desert environments* (pp. 303−332). Netherlands: Springer. Available from https://doi.org/10.1007/978-1-4020-5719-9_11.

Tuleya, R. E., DeMaria, M., & Kuligowski, R. J. (2007). Evaluation of GFDL and simple statistical model rainfall forecasts for United States landfalling tropical storms. *Weather and Forecasting*, *22*(1), 56−70. Available from https://doi.org/10.1175/WAF972.1.

Ushio, T., Sasashige, K., Kubota, T., Shige, S., Okamoto, K., Aonashi, K., Inoue, T., Takahashi, N., Iguchi, T., Kachi, M., Oki, R., Morimoto, T., & Kawasaki, Z. I. (2009). A Kalman filter approach to the global satellite mapping of precipitation (GSMaP) from combined passive microwave and infrared radiometric data. *Journal of the Meteorological Society of Japan*, *87*, 137–151. Available from https://doi.org/10.2151/jmsj.87A.137.

Vinukollu, R. K., Meynadier, R., Sheffield, J., & Wood, E. F. (2011). Multi-model, multi-sensor estimates of global evapotranspiration: Climatology, uncertainties and trends. *Hydrological Processes*, *25*(26), 3993–4010. Available from https://doi.org/10.1002/hyp.8393.

Wahid, A., Madden, M., Khalaf, F., & Fathy, I. (2016). Geospatial analysis for the determination of hydro-morphological characteristics and assessment of flash flood potentiality in Arid Coastal Plains: A case in Southwestern Sinai, Egypt. *Earth Sciences Research Journal*, *20*(1), E1–E9. Available from https://doi.org/10.15446/esrj.v20n1.49624.

Wang, S., Liu, J., Wang, J., Qiao, X., & Zhang, J. (2019). Evaluation of GPM IMERG V05B and TRMM 3B42V7 precipitation products over high mountainous tributaries in Lhasa with dense rain gauges. *Remote Sensing*, *11*(18). Available from https://doi.org/10.3390/rs11182080.

Wilcoxon, F. (1945). Individual comparisons by ranking methods. *Biometrics Bulletin*, *80*. Available from https://doi.org/10.2307/3001968.

Wu, Y., Zhang, Z., Huang, Y., Jin, Q., Chen, X., & Chang, J. (2019). Evaluation of the GPM IMERG v5 and TRMM 3B42 v7 precipitation products in the Yangtze River basin, China. *Water*, *11*(7). Available from https://doi.org/10.3390/w11071459.

Xie, P., Chen, M., & Shi, W. (2010). CPC global unified gauge-based analysis of daily precipitation. In *Preprints—24th conference on hydrology* (Vol. 2).

Xie, P., Janowiak, J. E., Arkin, P. A., Adler, R., Gruber, A., Ferraro, R., Huffman, G. J., & Curtis, S. (2003). GPCP pentad precipitation analyses: An experimental dataset based on gauge observations and satellite estimates. *Journal of Climate*, *16*(13), 2197–2214. Available from https://doi.org/10.1175/2769.1.

Xu, R., Tian, F., Yang, L., Hu, H., Lu, H., & Hou, A. (2017). Ground validation of GPM IMERG and TRMM 3B42V7 rainfall products over Southern Tibetan plateau based on a high-density rain gauge network. *Journal of Geophysical Research*, *122*(2), 910–924. Available from https://doi.org/10.1002/2016JD025418.

Yin, L., Zhou, Y., Ge, S., Wen, D., Zhang, E., & Dong, J. (2013). Comparison and modification of methods for estimating evapotranspiration using diurnal groundwater level fluctuations in arid and semiarid regions. *Journal of Hydrology*, *496*, 9–16. Available from https://doi.org/10.1016/j.jhydrol.2013.05.016.

Zhang, S., Wang, D., Qin, Z., Zheng, Y., & Guo, J. (2018). Assessment of the GPM and TRMM precipitation products using the rain gauge network over the Tibetan Plateau. *Journal of Meteorological Research*, *32*(2), 324–336. Available from https://doi.org/10.1007/s13351-018-7067-0.

Zhang, Z., Tian, J., Huang, Y., Chen, X., Chen., & Duan, Z. (2019). Hydrologic evaluation of TRMM and GPM IMERG satellite-based precipitation in a humid basin of China. *Remote Sensing*, *11*(4), 431. Available from https://doi.org/10.3390/rs11040431.

Precipitation Science

Measurement, Remote Sensing, Microphysics, and Modeling

Edited by

Silas Michaelides

A comprehensive work on the current state of research on precipitation, including coverage of recent discoveries, connections, and ways of improving accuracy.

Precipitation Science: Measurement, Remote Sensing, Microphysics, and Modeling addresses the latest key concerns for researchers in precipitation science: observing, measuring, modeling, and forecasting. Using case studies and global examples, this book demonstrates how researchers are addressing these issues using state-of-the-art methods and models to improve accuracy and output across the field. In the process it covers such topics as discrepancies between models and observations, precipitation estimations, error assessment, droplet size distributions, and using data in forecasting and simulations.

Precipitation Science presents an accessible synthesis of current knowledge in the field, including improved standard approaches, novel approaches, and coverage of a variety of topics such as climatology, data records, and more. By providing comprehensive coverage of the most up-to-date approaches to understanding, modeling, and predicting precipitation, this book offers researchers in atmospheric science, hydrology, climatology, and meteorology a comprehensive resource for improving their outcomes and advancing their knowledge.

Key features

- Provides updated and novel approaches to key issues in precipitation research
- Offers practical knowledge through global examples and case studies
- Includes full-color visuals to enhance comprehension of key concepts
- Embraces state-of-the-art instrumentation for recording precipitation

About the editor

Silas Michaelides, The Cyprus Institute, Climate and Atmosphere Research Center (CARE-C), Nicosia, Cyprus

Prof. Michaelides is a well-respected expert in meteorology and remote sensing with over 45 years of experience. Experienced in teaching, research, and management, his career has included being the Director of the Department of Meteorology of Cyprus, the Permanent Representative of Cyprus to the WMO, Representative of Cyprus to the European Organizations EUMETNET EIG and ECOMET EIG, and Associate Editor of the journals *Atmospheric Research* and *Heliyon*. He has over 270 publications including more than 120 peer-reviewed papers in international journals, 23 book chapters, and 30 edited and guest edited books and journals. His areas of interest include remote sensing applications to meteorology, dynamic meteorology, atmospheric energetics, climatology, weather radar, artificial neural network applications in atmospheric science, and weather forecasting.

ISBN 978-0-12-822973-6

9 780128 229736

ELSEVIER

elsevier.com/books-and-journals